2016

An examination of the reactivity of CO2 with Mg-silicates at pressures and temperatures of the earth's mantle and implications for deep carbon storage

Emily S. Devers

ABSTRACT

AN EXAMINATION OF THE REACTIVITY OF CO_2 WITH MG-SILICATES AT PRESSURES AND TEMPERATURES OF THE EARTH'S MANTLE AND IMPLICATIONS FOR DEEP CARBON STORAGE

Emily S. Devers, M.S.
Department of Geology and Environmental Geosciences
Northern Illinois University, 2016
Mark R. Frank, Thesis Director

The deep carbon cycle can be better constrained by understanding the reactivity of CO_2 with common mantle minerals. Surface reservoirs exchange carbon to the mantle via subduction zones, which carry carbonate minerals into the mantle. It is commonly accepted that there is a carbon deficiency with regards to degassing and the mantle may be the largest potential reservoir for terrestrial carbon. Carbon is released from decarbonation reactions as a volatile (i.e. CO_2) and may react with common mantle minerals including forsterite (end member Mg-olivine) to produce a carbonate mineral, magnesite, which has been shown to have exceptional stability under high pressure and temperature conditions.

The purpose of this study is to demonstrate a magnesite-forming reaction between forsterite and CO_2 using a high pressure diamond anvil cell with in-situ laser heating. Samples analyzed using micro X-ray diffraction definitively show the presence of magnesite at pressures ranging from 2.43 to 21.1 GPa and temperatures of up to 1590 K. These results indicate that magnesite can be produced through a forward reaction in the upper mantle and into the transition zone, and that carbon prefers a crystalline solid at these conditions over CO_2. Previous studies conducted at pressures less than 3 GPa suggest magnesite ($MgCO_3$) and enstatite ($Mg_2Si_2O_6$) as reaction products. This data show that at pressures from 2.43 to 15.8 GPa, magnesite forms in addition to a $Mg_2Si_2O_6$ phase and an SiO_2 phase. At pressures higher

than 15 GPa, $Mg_2Si_2O_6$ is no longer observed and magnesite and SiO_2 are the favored products. The results from this study indicate a complex reaction pathway as a function of structural changes in both products and reactants with increasing pressure. However, the presence of magnesite as a reaction product at the conditions of the upper mantle and transition zone show this phase is important as a deep carbon reservoir and may be a key factor in melt production at the core-mantle boundary and in the generation of carbonatite and kimberlitic magmas.

NORTHERN ILLINOIS UNIVERSITY

DEKALB, ILLINOIS

MAY 2016

AN EXAMINATION OF THE REACTIVITY OF CO_2 WITH MG-SILICATES AT PRESSURES AND TEMPERATURES OF THE EARTH'S MANTLE AND IMPLICATIONS FOR DEEP CARBON STORAGE

BY

EMILY S. DEVERS

A THESIS SUBMITTED TO THE GRADUATE SCHOOL

IN PARTIAL FULFILLMENT OF THE REQUIRMENTS

FOR THE DEGREE

MASTER OF SCIENCE

DEPARTMENT OF GEOLOGY AND ENVIRONMENTAL GEOSCIENCES

Thesis Director:
Professor Mark R. Frank

DEDICATION

This thesis is dedicated to my children, Addison and Theodore, whom I love unconditionally, even more than rocks.

ACKNOWLEDGEMENTS

I would like to acknowledge the support of my advisor, Dr. Mark Frank, throughout the entirety of this project. Dr. Frank has been a fantastic educator and much more throughout my time at Northern Illinois University. He has provided me with a pathway for scientific and critical reasoning which has allowed for my success in the geosciences and continues to be a guiding light in my everyday life as well. I owe my passion for geology to many professors in the Geology Department, with Dr. Frank at the top of this list. This project is a result of that passion. I would also like to thank my committee member Dr. Jim Walker, for his charismatic and intriguing classes as well as his contributions to this thesis. Additionally, I would like to thank committee member Dr. Nicole LaDue for her knowledge and contributions towards this project. Finally, I would like to acknowledge friends and colleagues, whom have made this office a joy to work in, whom have helped to create bonds that feel more like family than friends. I am appreciative of the support and contributions you continue to give me, towards this project and life. I would like to express gratitude and appreciation to my parents, who have never stopped supporting my dreams, and to my children, who shape my dreams and goals with their beautiful outlook on life and help me strive to be a better person, so that they can grow up in a world where science and learning is valued and respected.

TABLE OF CONTENTS

Page

Chapter Page

LIST OF TABLES

Table Page

LIST OF FIGURES

Figure Page

LIST OF APPENDICES

Appendix Page

CHAPTER I

INTRODUCTION

Carbon flux on a planetary scale is controlled by interactions between the deep Earth, near-surface, and surface reservoirs that have contributed to the evolution of the Earth's atmosphere and climate. Bulk Earth estimates of carbon concentrations are on the order of 0.1 wt. % or 730 ppm with a core concentration of up to 0.25 ± 0.15 wt. % through differentiation processes (Dasgupta, 2013). These estimates suggest that most of the primordial carbon not degassed to the atmosphere or lost to space was likely sequestered into the core during its formation. The Earth's mantle accounts for 83% (volume) and 67% (weight) of the Earth and, thus, represent a significant potential reservoir for carbon. There is a dearth of data on the present day concentration of carbon in the mantle; concentrations have been proposed to range from 30 to 1800 ppm, depleted vs enriched mantle concentrations, and are likely the result of hundreds of millions to billions of years of subduction of carbonaceous material into the planet's interior (Dasgupta, 2013).

Common carbonate minerals near the Earth's surface include but are not limited to: calcite ($CaCO_3$), aragonite ($CaCO_3$), dolomite ($CaMg(CO_3)_2$) and magnesite ($MgCO_3$). These minerals are common in reef systems, tidal flats, non-marine lakes, hot springs, evaporites, serpentized basalt/gabbro (Mg-rich), heavily fractured MORB, and sediments (Alt et al., 2012). Carbonates have also been observed in mantle-derived rocks which include kimberlites and carbonatites (Bailey, 1980).

Carbon can exist in the Earth's mantle as a volatile species (e.g., CO_2) and as accessory crystalline phases. Surface reservoirs exchange carbon to the mantle via subduction zones, which entrain and carry carbon-bearing minerals to depth. Subducting slabs release volatiles in the fore-arc and sub-arc region through dehydration and decarbonation reactions, thus, a large proportion of carbon volatiles are returned to surface reservoirs on relatively short time scales (Hermann et al., 2006; Poli et al., 2009; Shaw et al., 2003). The characteristics of the fluids generated in subduction zones has been an ongoing study of research in petrology and geochemistry, yet the extent and efficiency of CO_2 degassing from carbon-bearing phases is only poorly constrained. Dasgupta and Hirschmann (2007) report that the concentration of CO_2 in the upper mantle is on the order of 0.1 to 0.4 weight %, some of which is contributed from deep carbon reservoirs (Russell et al., 2012), suggesting the cycling of carbon to depths beyond arc volcanism. Thus, although sedimentary sequences can contain up to 25 wt. % C, the reactivity of carbon in the deep Earth is largely unconstrained.

Experimental studies have attempted to constrain the carbon budget of the Earth by determining the maximum depths to which carbonate minerals can be subducted before transforming to either a different carbon-rich mineral or breaking down completely and releasing CO_2 through decarbonation reactions. Relative stabilities of select carbonate minerals are depicted in Figure 1. Previous studies suggest that Ca-rich carbonates are stable up to 90 km depth. At intermediate depths of 60 to 120 km, dolomite is the stable phase and at greater depths, beyond 120 km, magnesite is the dominant phase (Dasgupta and Hirschmann, 2010). Mg-rich carbonate stability was examined by Boulard et al. (2011), showing how carbonates under high pressure (signifying subduction) react with Mg-rich mantle silicates to form new carbon bearing phases (e.g. magnesite, dolomite).

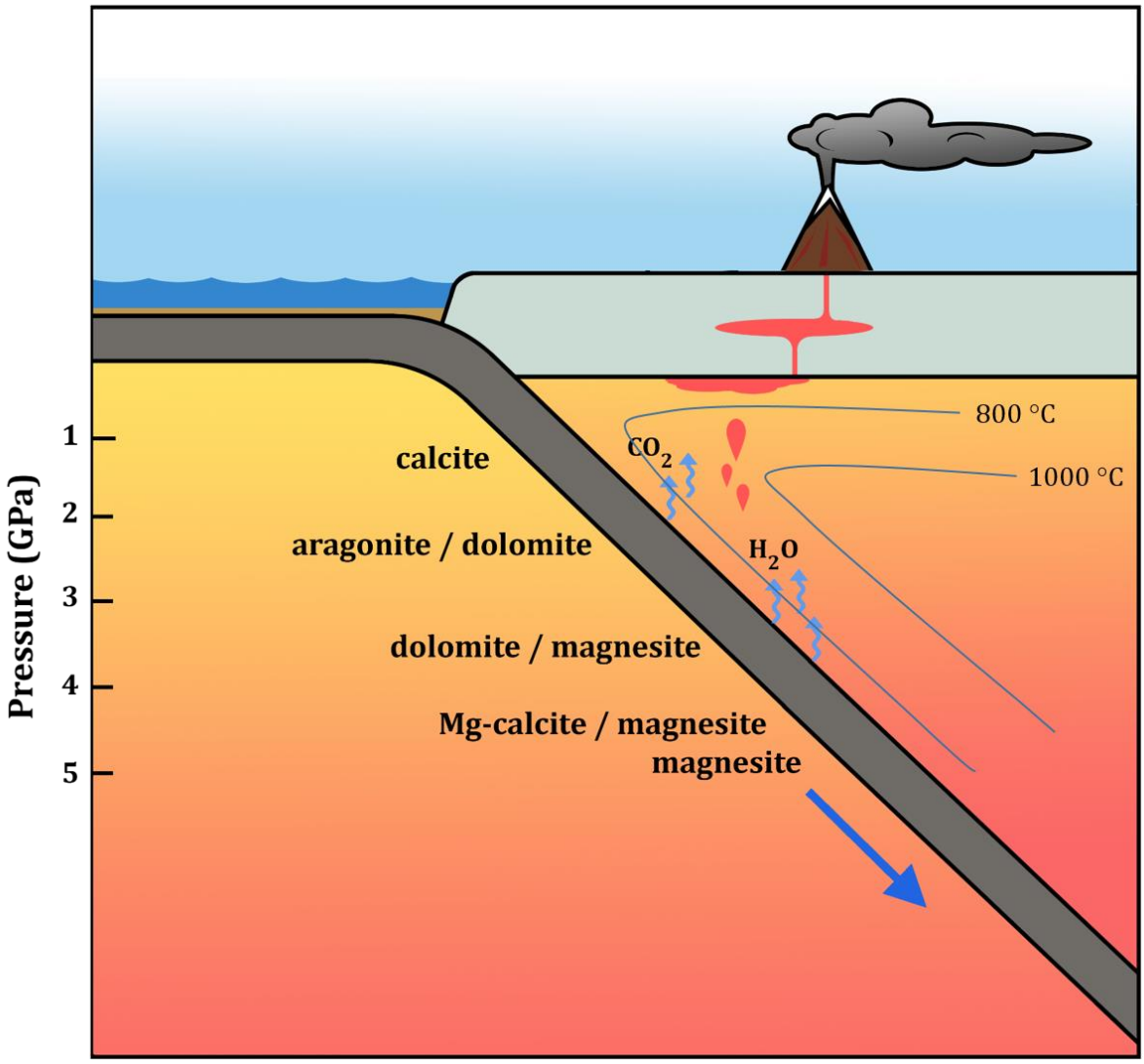

Figure 1. Schematic subduction zone showing the decarbonation of Ca-rich carbonates and the retention of Mg-rich carbonates. Magnesite is stable throughout the conditions shown on this schematic. Modified from Dasgupta and Hirschmann (2010).

As a result, magnesite is thought to be the dominant carbonate phase down to at least 660 km, thus, potentially making the mantle the largest potential carbon reservoir on a global scale. The phases that release CO_2 through decarbonation reactions play an important role in mantle melting as CO_2 can serve as a flux (Shaw et al., 2003). Furthermore, the liberation of H_2O-rich fluids during subduction greatly reduces carbonate stability as the solubility of CO_2 in H_2O increases with increasing pressure in a near 1:1 ratio up to 4.0 GPa (Ni and Keppler, 2013). The innermost portion of the slab contributes the most to the transfer of carbon to depth due to retention of cool temperatures and thus, increases carbonate stability. There is a currently acknowledged mass imbalance in the carbon cycle and is likely the result of carbon storage in the mantle as carbonate minerals (Dasgupta et al., 2004; Dasgupta and Hirschmann, 2007; Poli et al., 2009). This thesis seeks to explore the reactivity of CO_2, representing CO_2 produced through decarbonation reactions, with common mantle minerals at the pressures and temperatures typified by the Earth's geotherm.

Oxidation State of the Mantle and Evidence for Deep Carbonate

Magnesite can enter the mantle and resist decarbonation reactions because it is stable to temperatures greater than the Earth's geothermal gradient (Dasgupta et al., 2004). Even in the hottest subduction zones, the geotherm does not intersect the Mg-carbonate solidus (Figure 2). Although magnesite resists decarbonation at high temperature, carbon speciation and solubility are dependent on the oxygen fugacity (f_{O_2}) of the mantle**.** The upper mantle is most likely at an oxygen fugacity near the fayalite magnetite and quartz (FMQ) buffer, but it has also been suggested that the enstatite-magnesite-olivine-diamond (EMOD) buffer may

control the f_{O_2} of the upper mantle and transition zone (Berg, 1986). This range of f_{O_2} supports the hypothesis that CO_2 is the dominant volatile form of carbon in the upper mantle and transition zone and, when combined with the large stability field of magnesite, support the presence of carbonates in the upper mantle and transition zones.

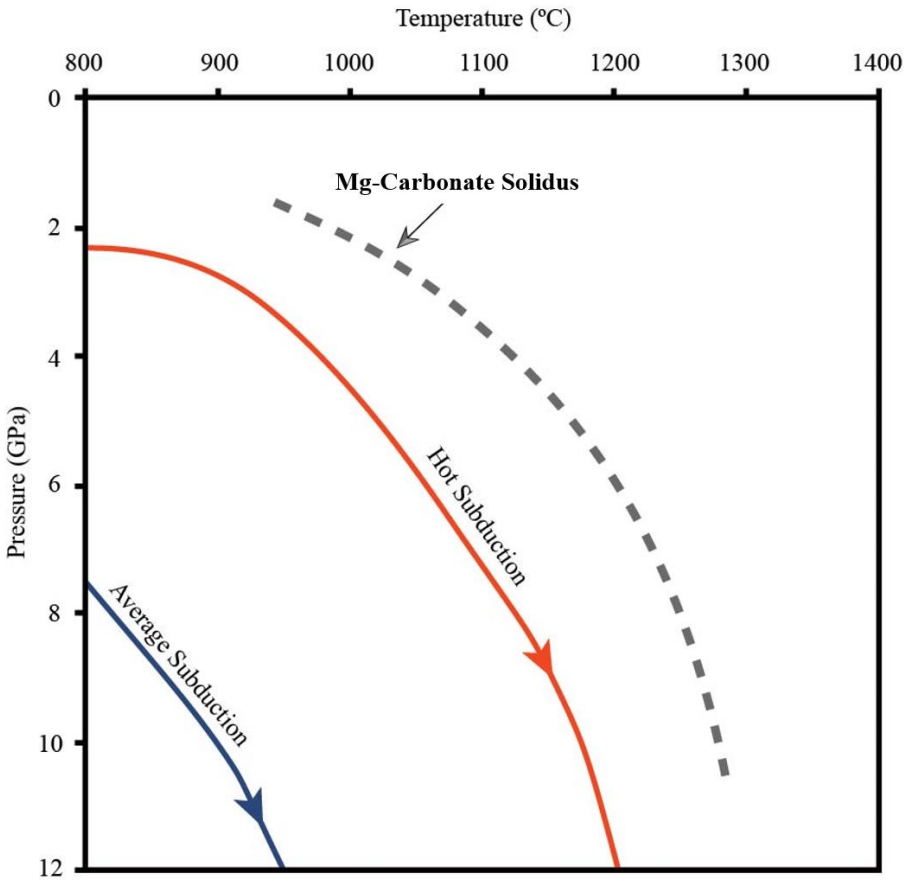

Figure 2. Mg-Carbonate solidus shown with geotherms for both hot and average subduction (modified from Dasgupta et al., 2004). The position of the Mg-carbonate solidus suggests this phase can withstand the pressures and temperatures present in all subduction zones.

Evidence for carbonate stability at depths greater than 50 GPa exists as carbonate preserved in inclusions in diamonds from the lower mantle. Brenker et al. (2007) have also identified primary carbonates hosted within diamond inclusions originating from the transition zone. Berg (1986) displayed novel evidence for carbonates present in mantle derived xenoliths in kimberlite magmas. The origin of these carbonates is likely from CO_2-enriched crustal and lithospheric material transported to great depths via subduction (Brenker et al., 2007). Furthermore, marbles and carbonated meta-sediments are preserved and associated with coesite-bearing metamorphic crustal rocks and represent remnants of subducted material. This suggests that natural rocks were altered in conditions that support carbonate stability.

Carbonates are more abundant relative to CO_2 as a host phase for carbon at the temperatures and pressures of the Earth's mantle (Koziol and Newton, 1998). Irving and Wyllie (1975) and Wyllie (1980) demonstrated that it is thermodynamically difficult to produce CO_2 through decarbonation at pressures up to 8.5 GPa. These thermodynamic data confirm that carbonates are the dominant C bearing phase within the upper mantle, and that in the presence of silicates, magnesite is the preferred carbonate (Boulard et al., 2011).

The fate of carbon in the lower mantle is, if possible, even less well known largely because there is little information of the fO_2 of the lower mantle (Stagno et al., 2011). The most supported hypotheses suggest the lower mantle has either a very low fO_2 due to interactions with the outer core (Frost et al., 2008) or a moderate to high fO_2 due to the supposed presence of Fe^{3+} in some silicate minerals and the buffering between carbonate and diamond (Stagno et al., 2011).

Dominant Mantle Phases

The bulk of the upper mantle is composed of olivine ($(Mg,Fe)_2SiO_4$), orthopyroxene (predominantly within the $Mg_2Si_2O_6$-$Fe_2Si_2O_6$ system) and clinopyroxene (predominantly within the $CaMgSi_2O_6$-$CaFeSi_2O_6$ system) in a ratio equivalent to a peridotite composition. Olivine, $(Mg,Fe)_2SiO_4$, changes structure with fluctuating pressure and temperature. As a result of increasing temperature a crystal's structure generally expands and increases in volume whereas pressure has an inverse effect. Forsterite (Mg_2SiO_4), the Mg-end member of olivine goes through several phase changes along the Earth's geotherm. In the Earth, the transition of forsterite to wadsleyite occurs at ~410 km (Fei and Bertka, 1999). This transition marks a structural change from orthorhombic to monoclinic crystal system and an increase in density, resulting in a volume reduction. From ~15-20 GPa depending on the geotherm, Mg_2SiO_4 is stable as ringwoodite. The transition of Mg_2SiO_4 from wadsleyite to ringwoodite occurs at ~520 km, within the transition zone. At higher pressures (~24 GPa), at the bottom of the transition zone and lower mantle, $MgSiO_3$ as bridgmanite is the preferred phase (Fei and Bertka, 1999).

$Mg_2Si_2O_6$ is present as orthoenstatite at ambient pressures and transitions to clinoenstatite, wadsleyite + stishovite, and majorite (Mg-bearing garnet) with increasing pressure (Figure 3). Phase equilibria for these transitions have been well studied (e.g., Hugh-Jones and Angel, 1994; Fei and Bertka, 1999); however, there is a dearth of data for the lattice parameters for these high pressure phases at pressures greater than approximately 9.0 GPa.

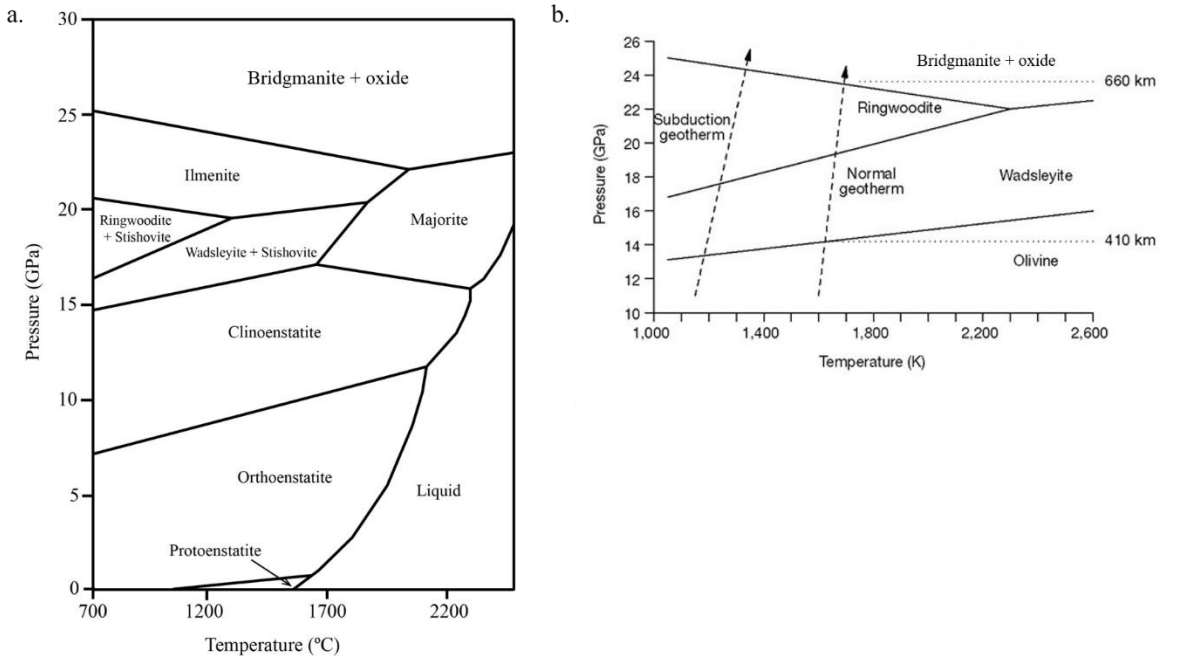

Figure 3. $Mg_2Si_2O_6$ and Mg_2SiO_4 phase diagrams. Pressure vs Temperature plot illustrating the boundaries for $Mg_2Si_2O_6$ polymorphs. Beyond ~15 GPa, $Mg_2Si_2O_6$ transforms into Mg_2SiO_4 at lower pressures and Majorite garnet at high pressure. b. Phase Diagram for Mg_2SiO_4 with average subduction and mantle geotherms to highlight dominant mantle phases at a given pressure and temperature. Modified from Fei and Bertka et al., 1999.

Previous Studies

Magnesite and a possible a high-pressure form of dolomite (Boulard et al., 2011) have been shown to resist decarbonation at mantle conditions and are the most likely reservoirs of carbon in the lower mantle. Volumetric constraints suggest the existence of free CO_2 gas in the lower mantle is limited (Ishikki et al., 2004). Conversely, Fiquet et al. (2002) utilized several thermodynamic parameters including free energies at standard state, P-T dependent entropies, and equations of state (EoS) for periclase (MgO), CO_2 and magnesite ($MgCO_3$) and concluded that volumetric constraints limit the formation of magnesite at high pressures and temperatures.

Experimental studies have contradicted the work of Fiquet et al. (2002) by using diamond anvil cells to monitor *in-situ* magnesite at high pressures and temperatures (Isshiki et al., 2004). These data showed the remarkable stability of magnesite up to 85 GPa and 3000 K, and even to depths of the D'' layer of the core-mantle boundary (CMB) (Isshiki et al., 2004). Recent experiments by Scott et al. (2013) furthered this research by illustrating that magnesite could form from the reaction of CO_2, produced through decarbonation reactions, with common mantle oxides. The reaction of CO_2 with MgO would readily produce magnesite at pressures of the upper mantle and transition zone, however, they also noted that the variations in the volumes of the CO_2 solid polymorphs (Figure 4) would limit, but not eliminate, this reaction at pressures greater than about 25 GPa. They hypothesized that the decrease in volume in the reactants, specifically that for CO_2, may slow magnesite formation at the high pressure found in the Earth's lower mantle.

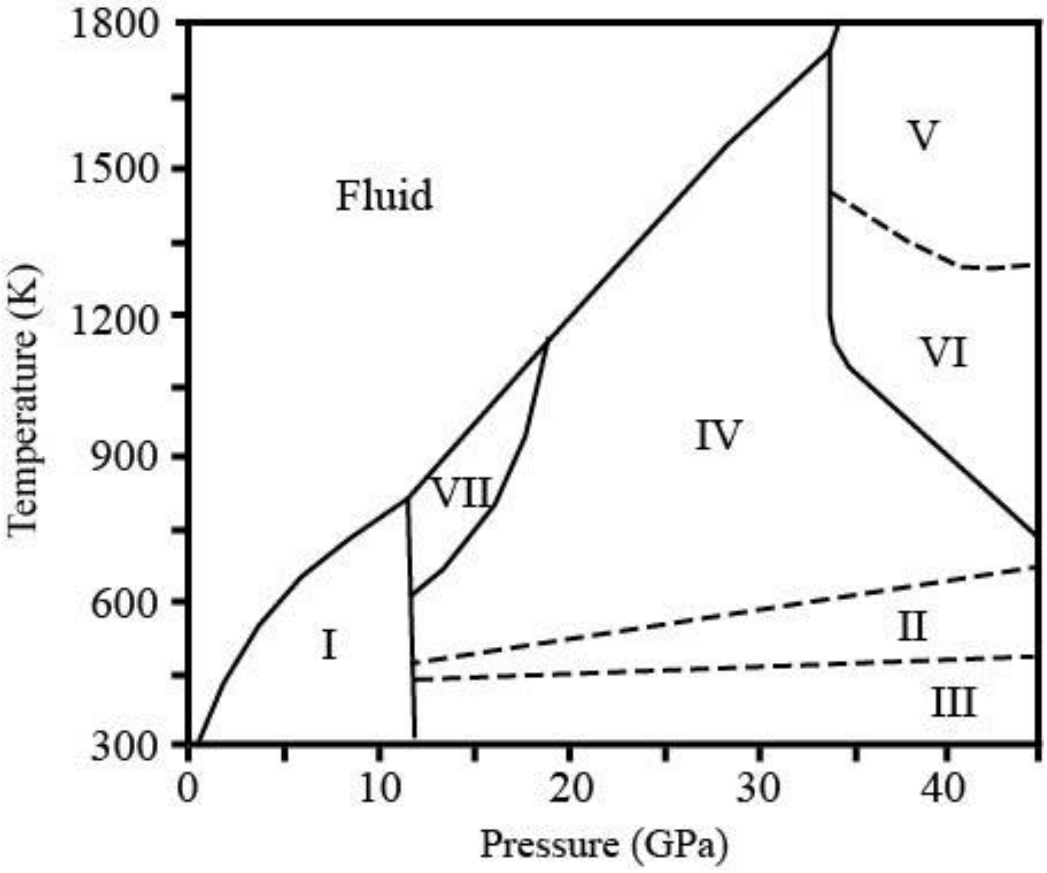

Figure 4. CO_2 phase diagram showing solid and fluid phase fields for carbon dioxide at variable pressure and temperature. Fluid field represents gaseous CO_2. Modified for simplicity from Litasov et al. (2011).

Currently, little experimental data exist on the potential reactivity of CO_2 with the dominant phases in the upper mantle (e.g. olivine, enstatite, diopside) and lower mantle (e.g. Mg, Fe-O, Mg-Si perovskites). Koziol and Newton (1998) conducted piston cylinder experiments up to 3 GPa (Figure 5) and suggested that Mg_2SiO_4 (forsterite) and CO_2 react to form $MgCO_3$ (magnesite) and $Mg_2Si_2O_6$ (enstatite). This study attempted to constrain the dominant reactions between forsterite (Mg_2SiO_4) and CO_2 as well as determine high pressure volume data for CO_2 and other phases produced. A thermodynamic model was established by using this new data in addition to the available standard state (at 1 bar) data published in Robie, Hemingway and Fischer (1978), in order to determine the most viable reaction occurring between forsterite and CO_2 between the pressure range of 0.43 to 21.1 GPa.

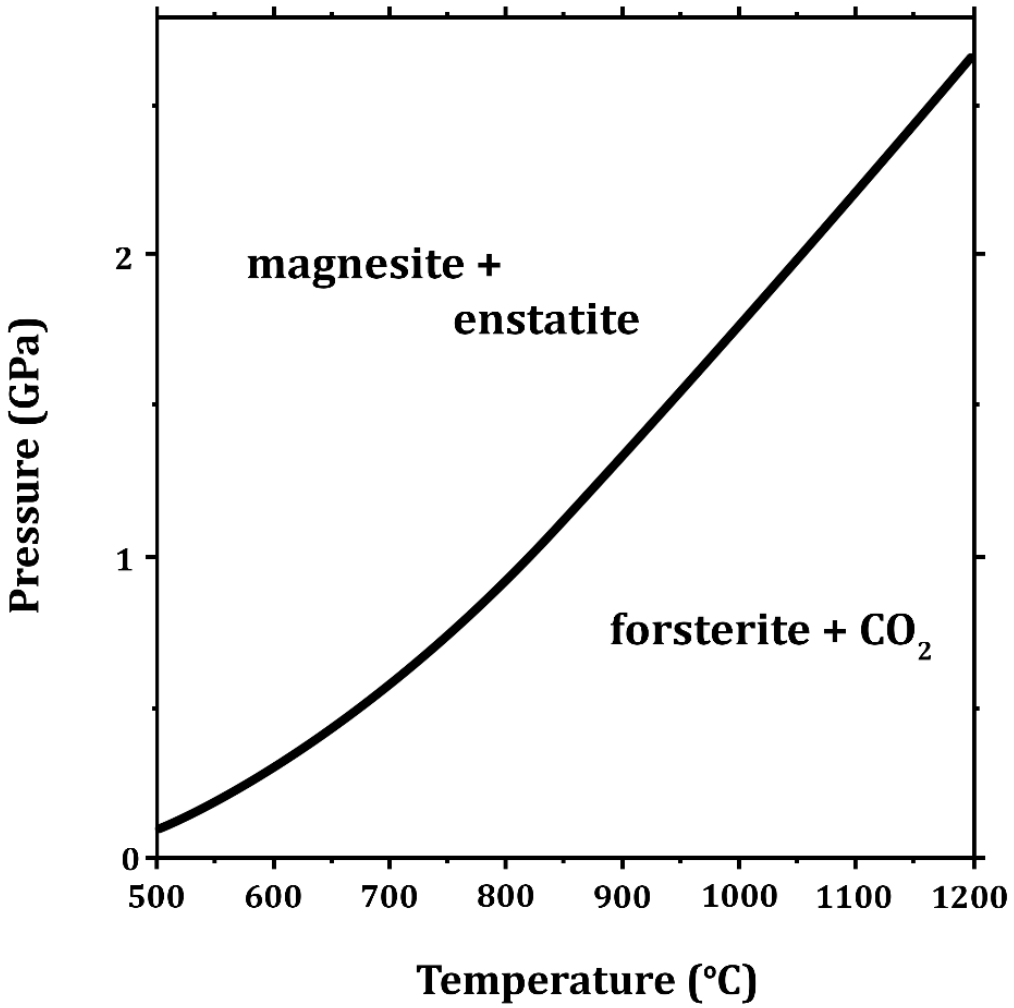

Figure 5. Pressure vs. Temperature diagram showing the equilibrium boundary between the reactants (forsterite + CO_2) and the products (magnesite + enstatite). Note that this phase diagram only extends to just over 2.5 GPa. Modified from Koziol and Newton, 1998.

CHAPTER II

EXPERIMENTAL DESIGN AND ANALYTICAL TECHNIQUE

Experimental Design

Experiments were conducted in symmetric diamond anvil cells (DACs) which compress the samples between two opposing diamond anvils to generate high pressures and are subsequently heated with Nd:YLF lasers. The diamonds were brilliant cut, type IIa, 2.35 and 2.38 mm in thickness, with culets of 250 μm. Two diamonds were aligned and cemented to tungsten carbide seats by using Resbond™ 940 zirconium high temperature cement. The seats were placed opposing each other within the DAC. Stainless steel gaskets were pre-indented between the diamonds to 40 μm thickness and a 100 μm diameter sample chamber was drilled into the gasket by using a Hylozoic Micro Electric Discharge Machining (EDM) System. The gaskets were then centered on the lower diamond and cemented for stability. The solid starting materials were placed into the drilled gasket holes and the DACs were closed in preparation for CO_2 gas loading (Figure 6).

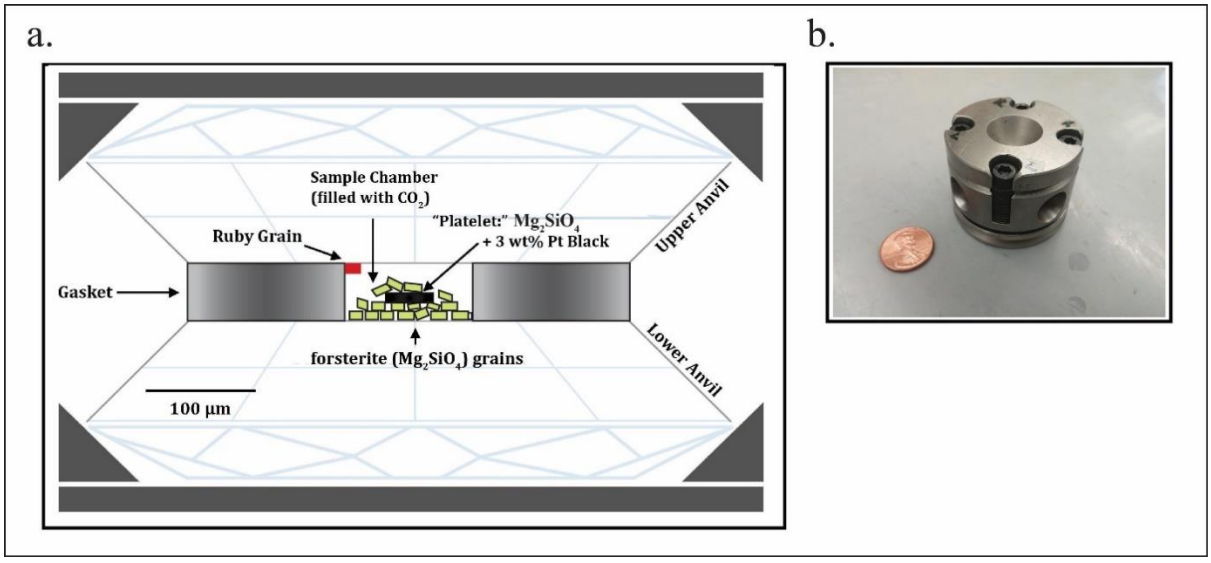

Figure 6. Diamond anvil cell schematic and photo. a) Schematic of a DAC with the loaded sample. The sample is contained within the drilled stainless steel gasket, with a ruby grain to measure pressure via ruby fluorescence. Modified from Scott et al., 2013. b) A picture of a loaded DAC with a penny for scale.

Starting Materials

Starting materials are listed in Table 1 and consisted of a 20:1 ratio by weight of pure forsterite (Mg_2SiO_4) and high purity platinum black, which was used to absorb infrared radiation during heating. The forsterite and Pt mixture was finely ground before being pressed between cutlets into a thin disc approximately 20 µm thick. Forsterite grains were placed at the top and bottom of the sample chamber to act as a barrier to avoid thermal contact between the diamond and the disc. The disc was placed above the forsterite grains in the center of the sample chamber (Scott et al., 2013). Multiple ruby grains of approximately 5 um diameters were placed along the edges of the sample chambers to be used as a pressure indicator through ruby fluorescence (Figure 6).

Table 1. Starting Materials and Composition

Starting Materials	Forsterite	CO_2	Platinum Platelet	Ruby Grain
Composition	Mg_2SiO_4 (synthetic, 99.9% pure)	Gas (99%)	3 wt.% Pt (99% pure) + Mg_2SiO_4	Cr-doped Al_2O_3

Analytical Technique

The prepared samples were taken to Argonne National Laboratory for CO_2 gas loading and analyses. The DACs were flooded with CO_2 gas by using the Gas Loading System at the GeoSoilEnviro Consortium for Advanced Radiation Sources (GSECARS) at Argonne National Laboratory's Advanced Photon Source (APS). The slightly open DACs were placed into a high-pressure vessel and pressurized to ~0.06 GPa with CO_2 at room temperature. The DACs were closed and pressurized to 1 GPa by remotely tightening the screws. The ruby grains were used to confirm the samples were under pressure before the DACs were removed from the gas loading apparatus. Raman spectroscopy was subsequently performed to confirm to presence of CO_2 within the sample chamber. Experiments were conducted at pressures and temperatures up to 21.1 GPa, and 1590 K, and subsequently quenched after a minimum of 15 second heating intervals at the highest temperatures (Table 2).

Table 2. X-ray Diffraction Pattern Number, Pressure and Temperature Conditions. Light blue, green and red coloration indicate pre-, *in-situ*, and post-heating patterns, respectively. Pressures are from ruby fluorescence measurements and temperatures are from Pt. Conditions in green represent XRD patterns from within the sample that were recorded during laser heating.

Pattern	P (GPa)	T (K)	Pattern	P (GPa)	T (K)
008	0.43 ± 0.03	298	100	11.7 ± 0.70	1050
010	0.43 ± 0.04	1750	104	11.7 ± 0.71	1500
017	0.48 ± 0.03	1620	108	15.4 ± 0.92	298
018	2.43 ± 0.15	298	110	15.4 ± 0.92	1350
049	2.43 ± 0.15	1460	115	15.4 ± 0.92	1260
050	2.43 ± 0.16	1570	116	15.4 ± 0.92	1240
060	6.10 ± 0.37	298	117	15.4 ± 0.92	1230
069	6.10 ± 0.38	1500	120	15.8 ± 0.95	1560
075	6.10 ± 0.39	1200	121	21.1 ± 1.27	298
083	9.00 ± 0.54	298	122	21.1 ± 1.27	1590
091	9.00 ± 0.54	1250	131	21.1 ± 1.27	1590
094	11.7 ± 0.70	298			

X-ray diffraction measurements were collected *in-situ* by using beamline 16-ID-B of the High-Pressure Collaborative Access Team (HPCAT) which utilizes micro-XRD angle-dispersive X-ray diffraction with a 3x5 μm beam as well as a double penetrating diode-pumped ytterbium-doped fiber laser heating system which heated a 20 μm diameter area (Figure 7). The results from this study will focus on pre- and post-heat patterns as the patterns collected during heating are much more difficult to constrain. Pressures were achieved by tightening bolts around the outside of the DAC. Once the sample is pressurized, it is laser heated to the temperature chosen for that pressure. It is important to note that the laser heating spot is constrained in both diameter and depth and the area being heated does not reach the

diamonds in the vertical directions and does not come in contact with the gasket in the lateral directions. High temperatures were achieved by using infrared spot heating within the sample up to 1600 K.

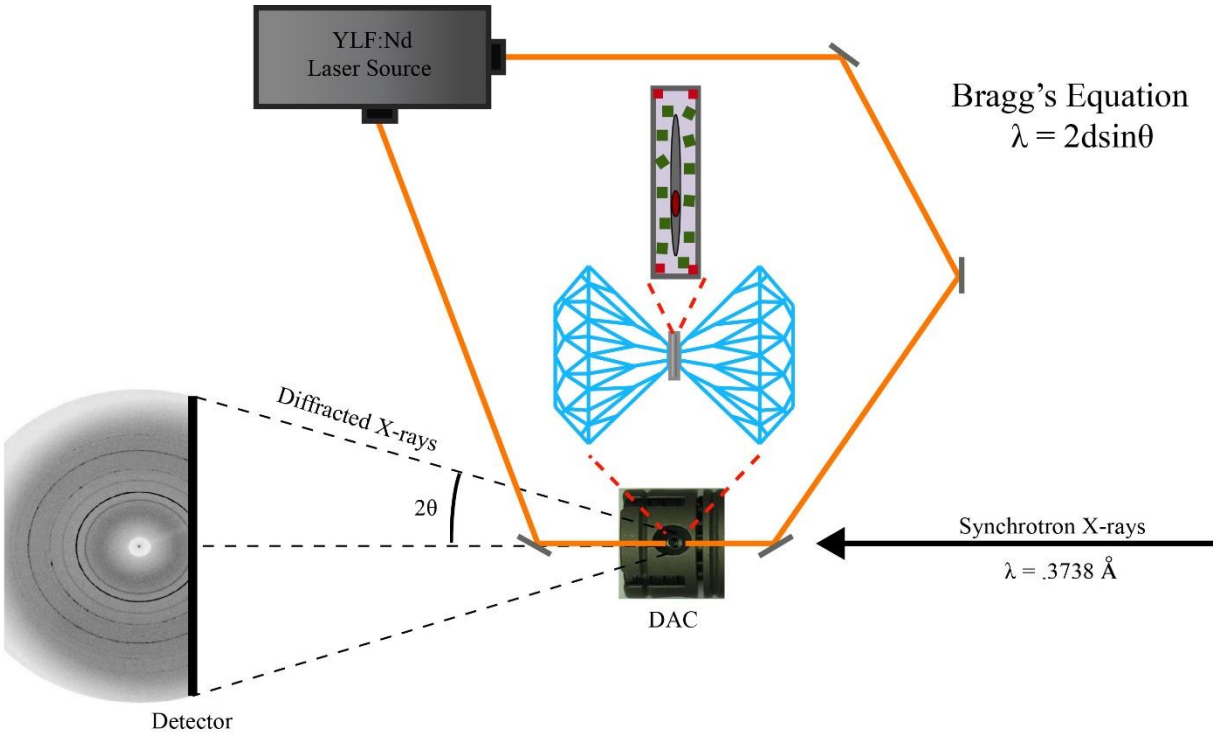

Figure 7. X-ray Diffraction and Laser Heating of a Diamond Anvil Cell showing the generation of a diffraction pattern. This schematic illustrates the direction of propagation for the X-ray and laser through the sample. The zoomed in sample chamber shows a red disc, symbolizing the heating spot produced by the lasers coupling with the Pt-black within the sample chamber.

Figure 8 shows heating spots (~20 µm) on the sample; allowing for the use of a single DAC for several experiments at different pressures and temperatures. Temperatures were estimated by using the visible portion of spectral radiance of the heating spot in the sample in accordance to Planck's law of black body radiation:

$$B_\lambda(\lambda, T) = \frac{2hc^2}{\lambda^5} \frac{1}{e^{\frac{hc}{\lambda kT}} - 1} \quad (1)$$

B_λ is the spectral radiance of a body, h is Planck's constant, c is the speed of light in the medium, lambda (λ) is the wavelength of the spectral radiance, k is the Boltzmann constant, and T is the absolute temperature of the body.

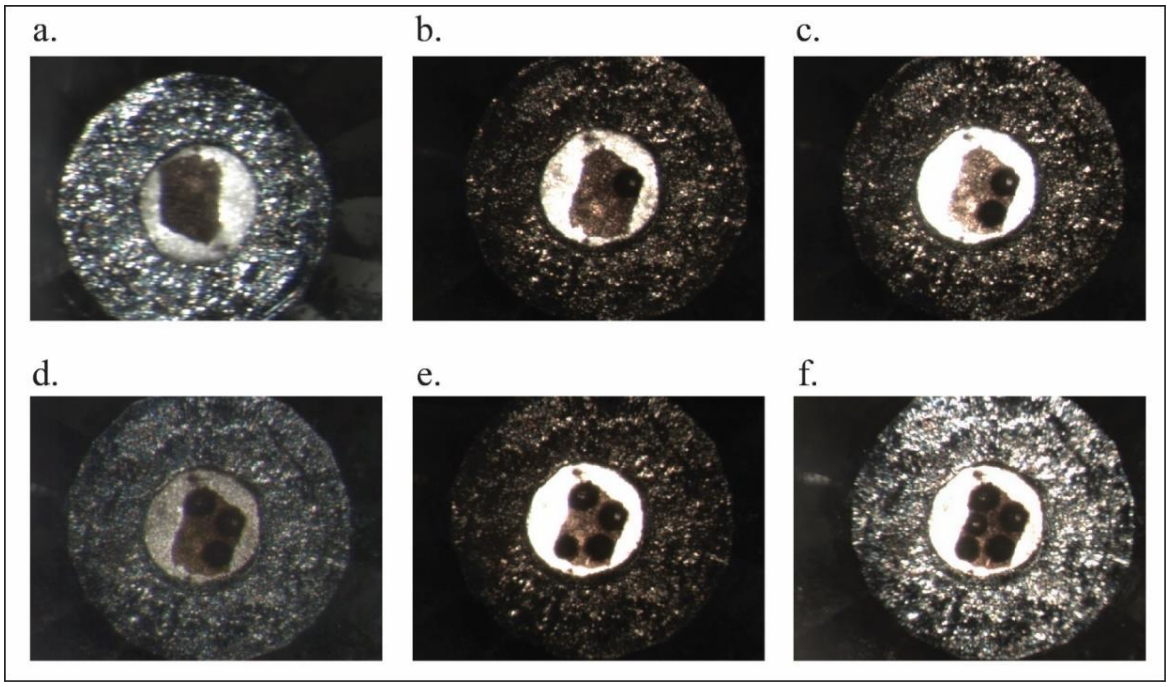

Figure 8. Spot heating of the sample using laser heating at varying pressures and photographed under a petrographic microscope. a.) A loaded cell with forsterite grain and CO_2, no heating at 0.43 GPa, b.) Heating cycle at 6.1 GPa, c.) Heating cycle at 9 GPa, d.) Heating cycle at 11.7 GPa, e.) Heating cycle at 15.4 GPa, and f.) Heating cycle at 21.1 GPa.

Ruby fluorescence was used as a pressure indicator for pre- and post-heat experiments for the total range in pressure (Mao et al., 1986). Ruby gave more accurate pre and post experiment pressures, especially at lower pressures; however, Pt was used as an internal pressure marker at elevated temperatures. The EoS of platinum was used to calculate the pressure throughout the experiments at the APS facility. Thus, two different pressure techniques were applied and are generally consistent. In this study pressures are reported as pre- and post-heat pressures measured using ruby fluorescence. This method has a ± 6% error associated with it, which is reported in Table 2.

Uncertainties in Platinum Pressure

Pressures were calculated at Argonne using the Pt equation of state (EoS). These values have been compared to pressures calculated by using the bulk modulus equation for magnesite with the volumes generated from this study. The calculated pressures for magnesite are slightly lower than the EoS method for Pt (Table 3). This may be due to thermal expansion which would produce calculated volumes that are higher than expected and as a result calculated pressures that are lower than expected. Platinum and the Pt-black platelet have a very low thermal expansion, and error from this factor would be negligible. Since Pt resists thermal expansion, it is a good indicator for pressures at elevated temperatures. However, in this study pressures are reported as pre- and post-heat, corresponding to pre- and post-heat X-ray diffraction patterns.

Table 3. Pressure Calibration Methods. Pressures determined from platinum EoS compared to pressures determined from magnesite bulk modulus equation.

P (GPa) Pt EoS Method	P (GPa) Mg K_o Method
2.43	2.43
6.1	4.39
9	9.25
11.7	9.94
15.8	11.6
21.1	18.8

Diffraction Technique and Pattern Generation

X-rays were focused on the sample before, during, and after laser heating. These X-rays were diffracted by the atomic planes within the sample at specific angles (θ), these angles can be used to calculate the d-spacing using Bragg's Equation:

$$\lambda = 2dsin\theta \quad (2)$$

Lambda (λ) is the wavelength of the incident wave, theta (θ) is the angle of incidence, and d-spacing (d) is a measurement of the distance between adjacent planes of a crystal lattice, which can be used to identify phases by their miller indices (hkl) and unit cell (abc).

Diffraction patterns were converted to one dimensional 2-theta or d-spacing data (with a correlated intensity) from a two dimensional image by using Fit2D software (Hammersley et al., 1996). Peak positions (d-spacings) and intensities for predicted phases were identified using previously published diffraction data (Angel et al., 2014; Fiquet et al., 2002; Giordano et al., 2010; Horiuchi and Sawamoto, 1981; Levien and Prewitt, 1981;

Periotto et al., 2012; Yoo et al., 1999). These data were used to match existing unit cell, miller indices, and relative intensity to the experimental values of this study to identify the phases present before and after heating of the sample.

Correcting for Peak Overlap

Overlapping and irregular shaped peaks were manually adjusted to a Gaussian profile and fit to a baseline (Figure 9) by using IgorPro software. Significant overlap occurs where a low intensity peak is masked by a higher intensity peak. It was especially important to correct for this so that less intense peaks could still be identified and used in unit cell calculations. Thus, peaks were identified and manually selected from the raw spectra, and a corrected spectrum with a baseline was generated.

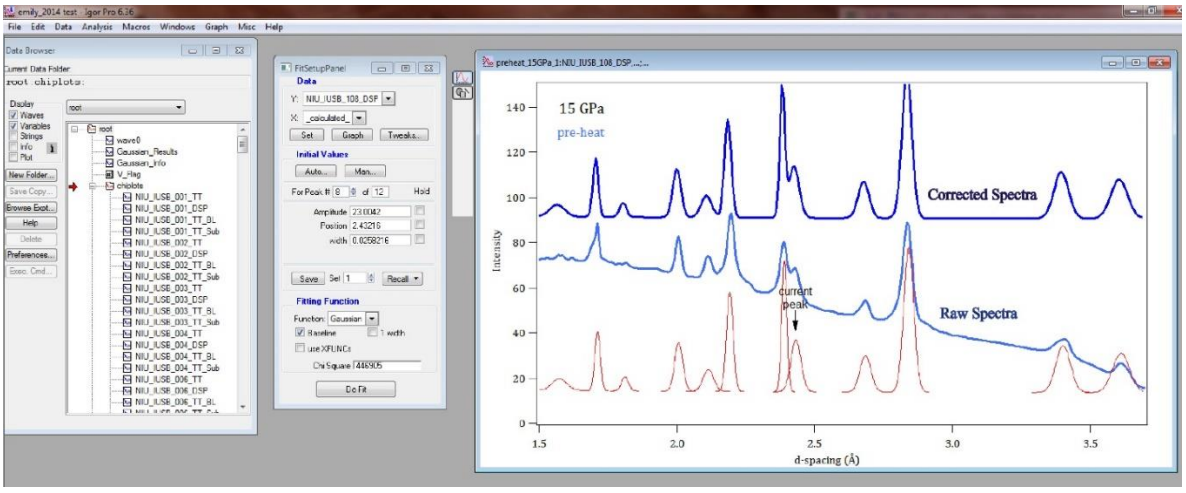

Figure 9. IgorPro window showing a sample of a successful Gaussian fit with a baseline. The manually chosen peaks of relative intensities are shown in red. The light blue pattern shows the irregular peaks and swaying intensity, the red peaks are those that are manually chosen, and the dark blue pattern is the Gaussian profile with a baseline, generated from diffraction pattern 108.

Unit Cell Calculation

Experimental d-spacings and reference miller indices (hkl values) were used to solve for the unit cell parameters. The calculated unit cell parameters and unit cell volume were obtained by using a macro generated for IgorPro software that allowed for input of the hkl parameters, determined d-spacing for each hkl, and the crystal system of the phase. The equations used for the calculations of the unit cell parameters are listed in Table 4.

Table 4. Crystal Systems and Unit Cell Equations.

Phase	Crystal System	Unit Cell Equation
Forsterite Wadsleyite CO_2-III Orthoenstatite	Orthorhombic	$\frac{1}{d^2} = \frac{h^2}{a^2} + \frac{k^2}{b^2} + \frac{l^2}{c^2}$
Ringwoodite CO_2-I	Cubic	$\frac{1}{d^2} = \frac{h^2 + k^2 + l^2}{a^2}$
CO_2-IV Magnesite Quartz	Hexagonal	$\frac{1}{d^2} = \frac{4}{3}\left(\frac{h^2 + hk + k^2}{a^2}\right) + \frac{l^2}{c^2}$
Stishovite	Tetragonal	$\frac{1}{d^2} = \frac{h^2 + k^2}{a^2} + \frac{l^2}{c^2}$
Coesite Clinoenstatite	Monoclinic	$\frac{1}{d^2} = \frac{1}{sin^2\beta}\left(\frac{h^2}{a^2} + \frac{h^2 sin^2\beta}{b^2} + \frac{l^2}{c^2} - \frac{2hlcos\beta}{ac}\right)$

Reference Minerals Used for Phase Identification

Samples were characterized at each projected heating spot prior to heating to verify that no premature reactions had occurred between the forsterite and CO_2. Forsterite was identified at all pressures by using reference d-spacing's from Birle et al. (1968). Although Mg_2SiO_4 goes through several high pressure phase changes (Fei and Bertka, 1999), forsterite reference d-spacings were used to identify the presence of all Mg_2SiO_4 pre-heat peaks. Forsterite crystallizes in the orthorhombic space group, with standard state unit cell parameters of a=4.762, b=10.225 and c=5.994 Angstroms (Å). These values along with a bulk modulus (K) of 135.7, and the derivative of the bulk modulus (K') of 3.98 were applied within the IgorPro XRD macro by using a third-order Birch-Murnaghan Equation of State to extrapolate the d-spacings to the conditions of these experiments, as a way to compare known XRD peaks to those in this study.

CO_2 was analyzed by using the same process, however, phase changes were incorporated. Data for phases I through III were used when available and necessary. High pressure CO_2 equilibria phase data were used as a first order approximation of what phase of CO_2 is expected at the conditions of interest. At low pressures and temperatures, CO_2-I crystallizes in the cubic crystal system where the unit cell parameters a, b and c = 5.84Å (Yoo et al., 1995; Giordano et al., 2010). At higher pressures CO_2-III crystallizes in the orthorhombic Cmca structure with unit cell parameters and equation of state of a=4.178, b=5.074, c=6.497 and K=25.161, K'=5.143 respectively (Yoo et al., 1995; Giordano et al., 2010). The phase boundary between CO_2-I and CO_2-III occurs at ~10 GPa, but the

equilibrium boundary is not well constrained (Teweldeberhan et al., 2012). CO_2-IV crystallizes in the hexagonal-rhombohedral crystal system and has cell parameters (a and c) of 8.793 Å and 10.60 Å (Datchi et al., 2009). CO_2-II and CO_2-V are additional high pressure and temperature phases that were not accounted for in this study.

Previous studies (Koziol and Newton, 1998; Scott et al., 2013) suggest a carbonate and a silicate phase are produced when forsterite reacts with CO_2 at high pressures and temperature. For this reason, reference unit cell data were also collected for magnesite ($MgCO_3$) and enstatite ($Mg_2Si_2O_6$) and high pressure $MgSiO_3$ phases (Angel et al., 1992a). Magnesite crystallizes in the hexagonal crystal system, and has unit cell parameters of 4.6339 (a and b) and 15.017 (c) (Fiquet et al., 2002; Ross, 1997).

Orthoenstatite is a low pressure $Mg_2Si_2O_6$ phase that crystallizes in the orthorhombic (Pbca) crystal system (Hugh-Jones and Angel, 1994); with abc parameters of 17.977, 8.67, and 5.1227, respectively, and with a K of 105.8 and a K' of 8.5 (Angel and Jackson, 2002). Clinoenstatite is monoclinic with cell dimensions of 9.201, 8.621, and 4.908 Å for a, b, and c, respectively. At pressures greater than ~15 GPa, $Mg_2Si_2O_6$ transforms into high pressure Mg_2SiO_4 + SiO_2 phases, present as ringwoodite + stishovite, or wadsleyite + stishovite as pressure increases to 15 and 21 GPa, respectively. Wadsleyite forms in the orthorhombic system (Im2a space group), cell dimensions are a = 5.6983, b = 11.4380, and c = 8.2566 Å (Horiuchi and Sawamoto, 1981). Ringwoodite is within the cubic system with a unit cell parameter of 8.12Å (Bauer, 1972). Stishovite has tetragonal symmetry with cell parameters a = 4.1801Å, and c=2.6678 Å (Ross et al., 1990). Additionally, quartz unit cell parameters were collected for room temperature SiO_2 using EoS and XRD data from Angel et al. (1997). Unit

cell parameters for high pressure phases were collected from various sources at the pressure of interest at a range of temperatures. The values selected from these sources closely approximate the conditions of this study, and as such, are viable for comparison to the data from this study. These minerals will be used as a reference for experimental d-spacings from this study, and used to identify the peaks of reaction products.

Uncertainties

Uncertainties in the identification of mineral phases using previously determined experimental data are reported as the difference between d-spacings (Δd). These values are less than 0.03 Å in all experiments. Uncertainty in the unit cell calculations are calculated by determining the standard deviation from the mean for each unit cell parameter (abc). Unfortunately, in XRD patterns with too few high intensity d-spacing peaks, there were not enough data points to determine the deviation. In this case, there is no associated error with the unit cell calculation. Unit cell volumes were also calculated as 1σ standard deviation from the mean.

CHAPTER III

RESULTS

This study focused on identifying pre- and post-heat phases by using XRD patterns and the d-spacing measurements from the literature of all possible phases. The d-spacing values ascertained from the experiments also allowed for unit cell parameters and volumes to be calculated where possible at pressures and temperatures reflecting the Earth's upper mantle and transition zone, 0.43 to 21.1 GPa and up to 1500 K. Observed d-spacing's in this study were compared to measurements from several other studies with reference d-spacing's that vary by ± 0.03 Å or less from the observed d-spacings of this study (Angel et al.,1992a; Angel and Jackson, 2002; Birle et al. 1968; Bauer, 1972; Fiquet et al., 2002; Giordano et al., 2010; Horiuchi and Sawamoto, 1981; Hugh-Jones and Angel, 1994; Yoo et al., 1995; Ross et al., 1990; Teweldeberhan et al., 2012). The phases listed in Table 4 are representative of the highest intensity peak for each phase on an individual XRD pattern (data for all peaks are available in Appendix A). The highest intensity peak is often associated with the same hkl for any given phase, but grain orientations within the cell can increase or decrease the relative intensity of a given peak as the crystal undergoes Laue style diffraction. Whereas the relative intensity of a peak may vary, the d-spacing for that same peak is unchanged at any given temperature and pressure. Thus, these diffraction peaks (or lines) can be used to identify the presence of any given phase even with varying orientations within the sample. For example, in experiment 008, the highest counts (intensity) occurred at a d-spacing of 2.769 Å, which is indicative of a forsterite-bearing phase.

Observed D-Spacing for Pre- and Post-Heat Phases

Mg_2SiO_4 was observed in all pre-heat XRD patterns with highest intensity peaks ranging from 2.411 to 2.933 Å with a Δd of 0.01 Å or less. CO_2 was not present in the XRD patterns at pressures below 1.0 GPa (008 and 017) because it existed as a liquid. In pre-heat patterns from 2.4 to 9.0 GPa, CO_2-I was measured and the highest intensity peaks decreased in d-spacing from 3.11 to 2.128 (at 6.1 GPa) due to compression of the lattice. From 11.7 to 21.1 GPa CO_2-IIIwas present in pre-heat experiments with the highest intensity peaks corresponding to d-spacings of 2.880, 2.006 and 1.939 Å with hkls of 220 and 112, respectively. CO_2-IV is present in post-heat patterns from experiments at 15.8 and 21.1 GPa.

Magnesite ($MgCO_3$) peaks were observed in all post-heat experiments from 1.8 to 21.1 GPa with the observed d-spacings within 0.02 Å of the literature values (Fiquet et al., 2002). Since magnesite was not loaded into the DACs, the presence of magnesite could only be a result of the reaction of forsterite with CO_2. Thus, magnesite will form from the reaction of forsterite with CO_2 in the Earth's upper mantle and transition zone.

Orthoenstatite ($Mg_2Si_2O_6$) was another reaction product observed in post-heat experiments 049 and 075 at 1.8 and 6.4 GPa, respectively, and are in good agreement with reference orthoenstatite d-spacing data with $\Delta d < 0.01$ Å (Hugh-Jones and Angel, 1994). Clinoenstatite was the stable configuration of $Mg_2Si_2O_6$ from 9 to 11.7 GPa and had a Δd of 0.017 Å or less when compared to Angel et al. (1992). $Mg_2Si_2O_6$ was not observed in the XRD patterns at 15.8 GPa as wadsleyite (Mg_2SiO_4) and stishovite (SiO_2) become the dominant silica-rich phases. The data from experiments at 21.1 GPa also suggest ringwoodite and stishovite are the stable forms of Mg_2SiO_4 and SiO_2, respectively (Table 5).

Table 5. Pre- and Post-Heat phases and Lattice Parameters; Including Observed and Reference d-spacing values, calculated Δd, and Miller Indices. All d-spacing measurements are in Angstroms (Å).

Pattern	P (GPa)	Phase	Observed d-spacing	Reference d-spacing	Δd	h	k	l
008	Pre: 0.43	Forsterite	2.769	2.768	0.001	1	3	0
017	Post: 0.48	Forsterite	2.774	2.768	0.006	1	3	0
018	Pre: 2.43	Forsterite	2.755	2.756	0.000	1	3	0
		CO_2-I	3.111	3.074	0.037	1	1	1
049	Post: 1.80	Magnesite	2.737	2.722	0.016	1	0	4
		Orthoenstatite	3.127	3.129	0.002	2	2	1
		Quartz	3.286	3.283	0.003	0	1	1
		Forsterite	3.479	3.483	0.004	1	1	1
060	Pre: 6.1	Forsterite	2.755	2.756	0.000	1	3	0
		CO_2-I	2.128	2.072	0.056	2	1	1
075	Post: 6.4	Magnesite	2.082	2.066	0.016	1	1	3
		Orthoenstatite	3.116	3.120	0.004	2	2	1
		Coesite	1.753	1.755	0.002	2	0	4
		Forsterite	2.254	2.241	0.013	1	2	2
083	Pre: 9.0	Forsterite	2.933	2.939	0.006	0	0	2
		Ruby	2.068	2.062	0.005	1	1	3
091	Post: 9.0	Magnesite	2.249	2.259	0.009	1	1	0
		Clinoenstatite	2.071	2.066	0.005	5	0	2
		Coesite	2.693	2.693	0.000	2	2	0
		Forsterite	2.287	2.274	0.013	2	1	0
094	Pre: 11.7	Forsterite	2.411	2.402	0.009	1	1	2
		CO_2-III	2.880	2.816	0.065	1	1	1
104	Post: 11.1	Forsterite	2.670	2.704	0.034	1	3	0
		Magnesite	1.650	1.647	0.003	1	1	6
		Clinoenstatite	2.274	2.258	0.017	1	3	1
108	Pre: 15.4	Forsterite	2.842	2.905	0.063	0	0	2
		CO_2-III	2.006	1.992	0.014	2	0	0
120	Post: 15.8	Magnesite	2.650	2.628	0.023	1	0	4
		Wadsleyite	2.175	2.167	0.008	0	3	3

(Continued on following page)

Table 5. (Continued)

		Stishovite	2.917	2.913	0.004	1	1	0
		CO_2-III	1.939	1.946	0.007	1	1	2
		CO_2-IV	2.036	2.041	0.005	2	2	0
121	Pre: 21.1	Forsterite	2.665	2.661	0.004	1	3	0
		CO_2-III	2.114	2.110	0.004	1	1	2
131	Post: 21.1	Magnesite	1.614	1.597	0.018	0	1	3
		Ringwoodite	1.797	1.794	0.002	3	2	1
		Stishovite	2.232	2.205	0.027	1	0	1
		Forsterite	2.663	2.661	0.002	1	3	0
		CO_2-III	2.713	2.720	0.007	1	1	1
		CO_2-IV	2.036	2.041	0.005	2	2	0

*** All phases represent highest intensity peaks from the listed XRD pattern.**
*** Pressures are taken from Ruby Fluorescence measurements.**

Phases Observed in XRD Patterns

The X-ray diffraction patterns presented in Figures 10-16 are displayed as d-spacing (Å) vs Intensity (arbitrary units). The diagrams show diffraction patterns from the experiment prior to heating (pre-heat) that contain reactants only and after laser heating patterns (post-heat) that contain the reactants and any new phases produced through a reaction (products). The phases were identified by comparing the pre- and post-heat patterns to those from past studies on these phases. The pre-heat and post-heat XRD patterns at 0.43 and 0.48 GPa, respectively, contained only the reactants and no new phases (products) suggesting that forsterite and CO_2 are stable together and that no reaction occurred (Figure 10). All of the peaks of these patterns can be identified as forsterite or Pt (pressure indicator) because CO_2 is present as a liquid at these conditions and, therefore, will not produce a diffraction pattern.

Conversely, reaction products were observed at all other pressures, 2.43-21.1 GPa. Figures 11 through 16 depict pre- and post-heat XRD patterns with peaks indicative of magnesite, a product of the reaction of forsterite, the source of Mg and O, and CO_2, the source of CO_3^{-2}. At pressures lower than 15 GPa, additional phases present after laser heating include $Mg_2Si_2O_6$ and SiO_2. Patterns recorded at pressures ≥ 15 GPa demonstrate a structural transition trending from Mg_2SiO_4 as forsterite towards Mg_2SiO_4 as wadsleyite or ringwoodite and an $Mg_2Si_2O_6$ phase was no longer found in the pattern.

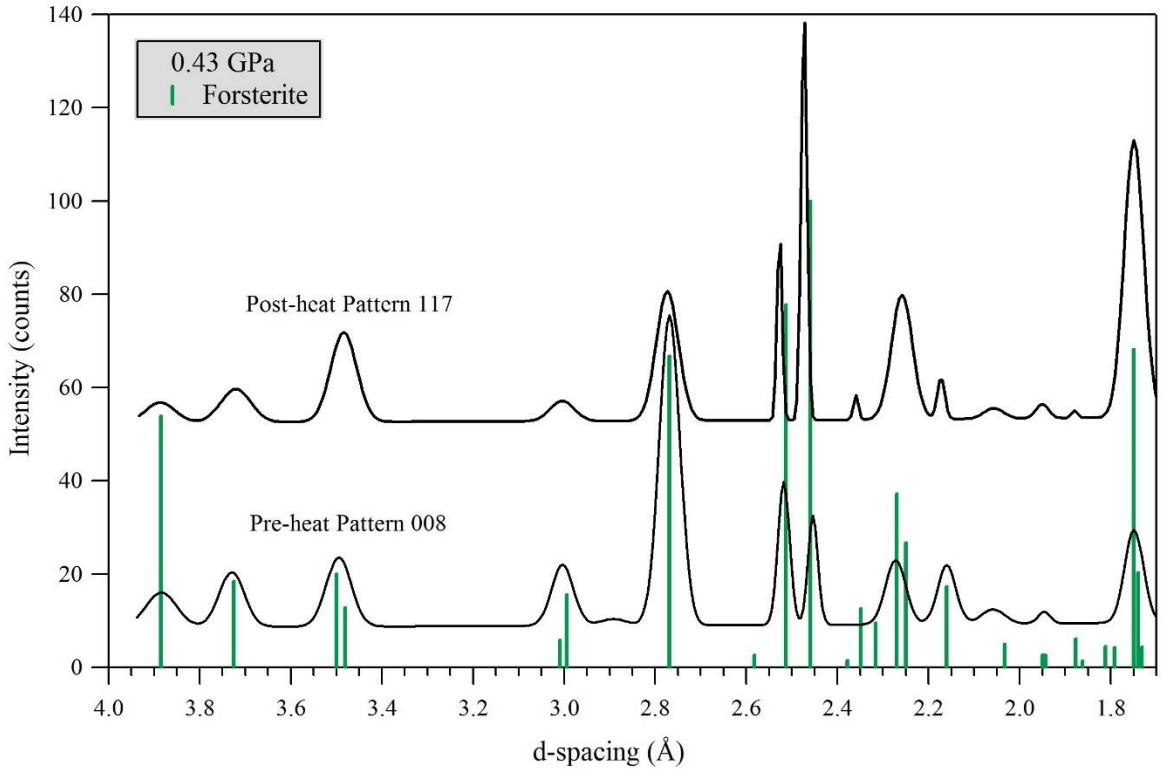

Figure 10. Pre- and post-heated X-ray diffraction patterns at 0.43 GPa. Patterns 008 and 017 only have forsterite present at these conditions. Magnesite formation was not observed at atmospheric pressures, even at high temperatures.

The experiment conducted at 2.43 GPa (Figure 11) showed new peaks at several d-spacing intervals with the highest intensity peaks at 2.089, 2.737, 3.127 and 3.286 Å. These new peaks represent magnesite (Fiquet et al., 2002), orthoenstatite (Hugh-Jones and Angel, 1994), and quartz (Angel et al., 1997), respectively. There was significant peak overlap which made it difficult to obtain d-spacings for all peaks in the patterns. For example, the peak at 2.737 Å in pattern 049 may appear to be the shifted forsterite peak at 2.755 Å in pattern 018, however, the growth of smaller intensity magnesite peaks supports the near complete reactivity of forsterite at the expense of magnesite formation, despite the peaks having a similar d-spacing, they are representative of the post-heat phases indicated. The three small peaks at the end of XRD pattern 049 represent unreacted forsterite, with CO_2 acting as the limiting reagent. It is also possible that the X-ray passed through an area of the sample chamber that is outside or at a greater depth than the area laser heated, therefore, not involved in the reaction.

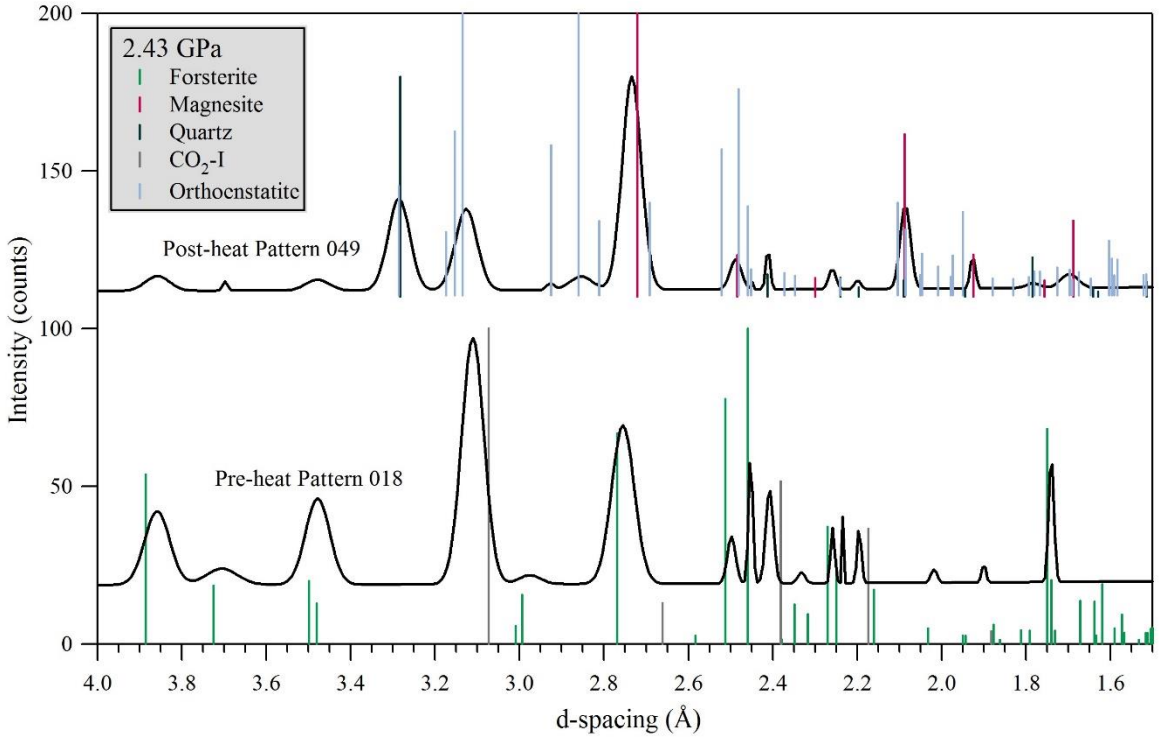

Figure 11. Pre- and post-heated X-ray diffraction patterns at 2.43 GPa. Post-heat patterns show magnesite, orthoenstatite and quartz formation, as well as residual un-reacted forsterite.

A phase change from quartz to coesite in post-heat experiments at 6.4 GPa is observed as new peak growth denoted at 3.053 and 3.377 Å (Figures 11 and 12). CO_2-III is also observed in pre-heat patterns at 6.1 GPa. Post-heat patterns at these pressures did not quench a solid CO_2 phase. This could suggest that all of the CO_2 was heated to a fluid, and was completely reacted away, or there was no CO_2 in the vicinity of the passing X-ray during experimental analysis.

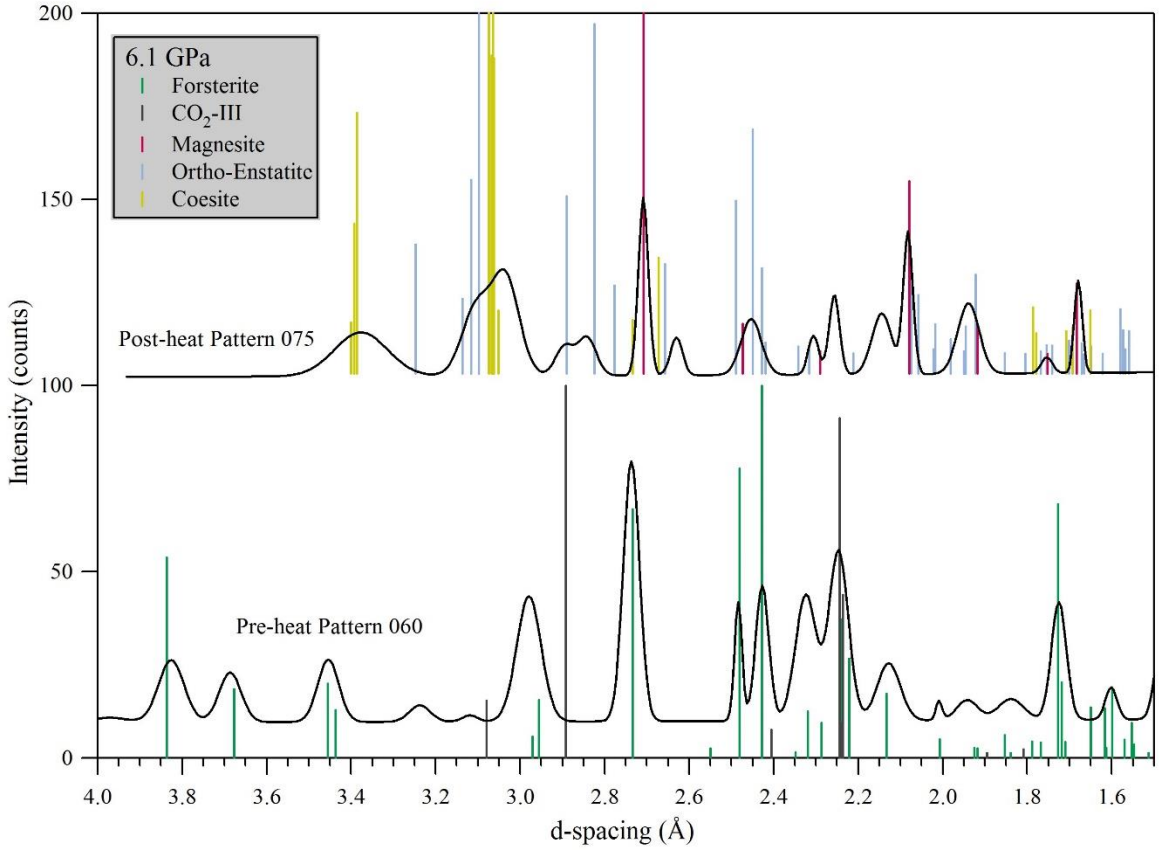

Figure 12. Pre- and post-heated X-ray diffraction patterns at 6.1 GPa. Pre-heat pattern show CO_2-III peaks and post-heat patterns indicate where coesite and orthoenstatite were observed as SiO_2 and $Mg_2Si_2O_6$ phases.

9.0 GPa post-heat experiments demonstrated a phase change from orthoenstatite to clinoenstatite with new peak growth at 1.912 and 1.949 Å. There was also a high intensity ruby peak at 2.068 Å observed in pre-heat pattern 060. Ruby grains were loaded into the corner of the sample chamber and may have migrated during the experiments or be hit by diffracted X-rays. This is the only pattern where ruby was observed. Observed magnesite

peaks are negligibly shifted (by less than 0.01 Å) from the measured magnesite reference peaks suggested by other studies (Figure 13).

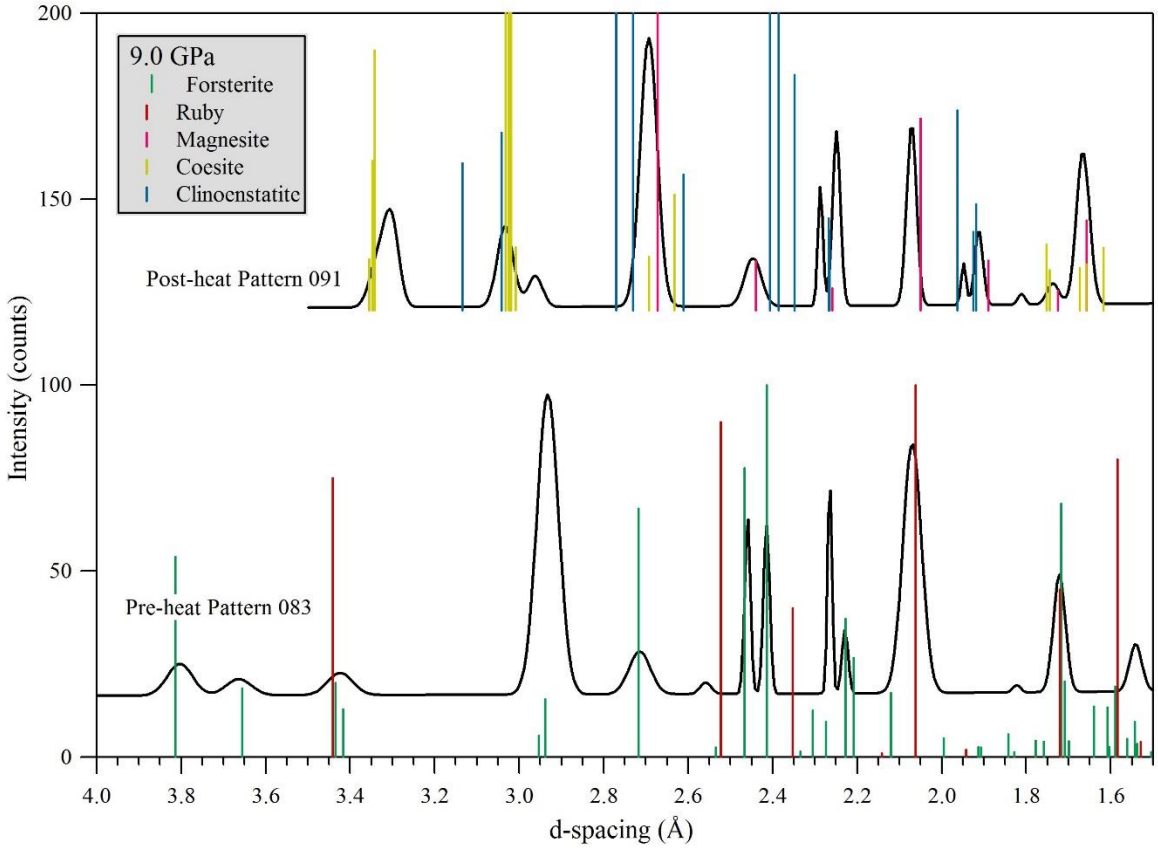

Figure 13. Pre- and post-heated X-ray diffraction patterns at 9.0 GPa. Pre-heat pattern 083 illustrate the positioning of forsterite peaks and a high intensity ruby peak. $Mg_2Si_2O_6$ was present as clinoenstatite and SiO_2 was present as coesite in post-heat pattern 091.

Forsterite peaks are consistent with previous pressures and are easily measured in pre-heat patterns at 11.7 GPa (Figure 14). Peaks indicative of CO_2-III are seen at the same pressure (in pattern 094) at 2.028 and 2.880 Å. SiO_2 has transitioned into stishovite which has

easily recognizable peaks at 1.513, 1.849 and 2.928 Å. $Mg_2Si_2O_6$ is present at clinoenstatite which is similar to $Mg_2Si_2O_6$ peaks at 9.0 GPa. There is a shift in the positioning of the observed magnesite peaks at 2.053 and 2.670 Å. These peaks have a d-spacing 0.023 Å larger than the reference peaks with which they are matched.

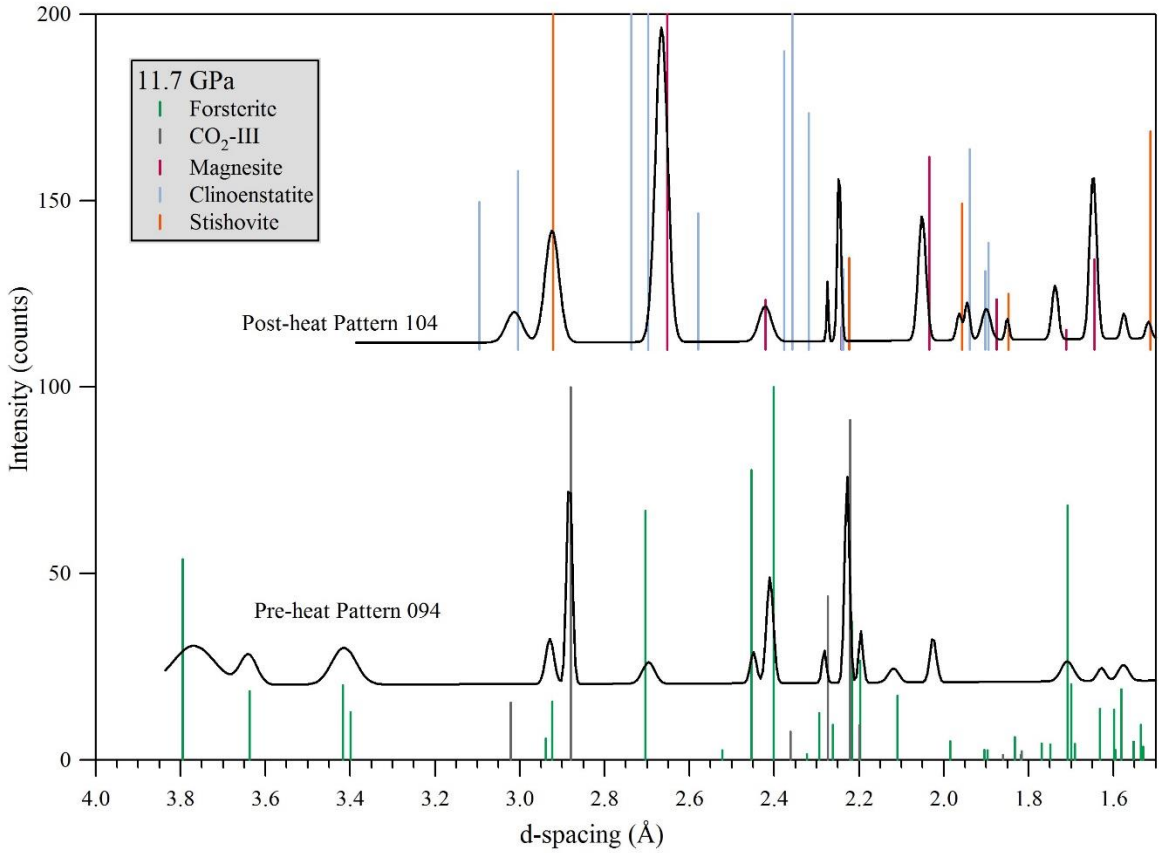

Figure 14. Pre- and post-heated X-ray diffraction patterns at 11.7 GPa. Peaks indicative of CO_2-III were evident in pre-heat patterns. Post-heat patterns show a transition from coesite to stishovite. Additionally, there appears to be a shift in d-spacing between measured and observed magnesite peaks due to thermal expansion.

Wadsleyite, a high pressure Mg_2SiO_4 phase, peaks are recorded at 1.954, 2.435, and 2.543 Å in experiments at 15.8 GPa (Figure 15). In the same experiment, CO_2 has quenched in the hexagonal crystal system with CO_2-IV peaks visible at 2.036 and 2.175 Å. Magnesite peaks were consistent with the d-spacing values published in the literature. Stishovite was the high pressure SiO_2 phase visible in experiments at this pressure, with peaks noted at 1.508, 1.837 and 2.917 Å.

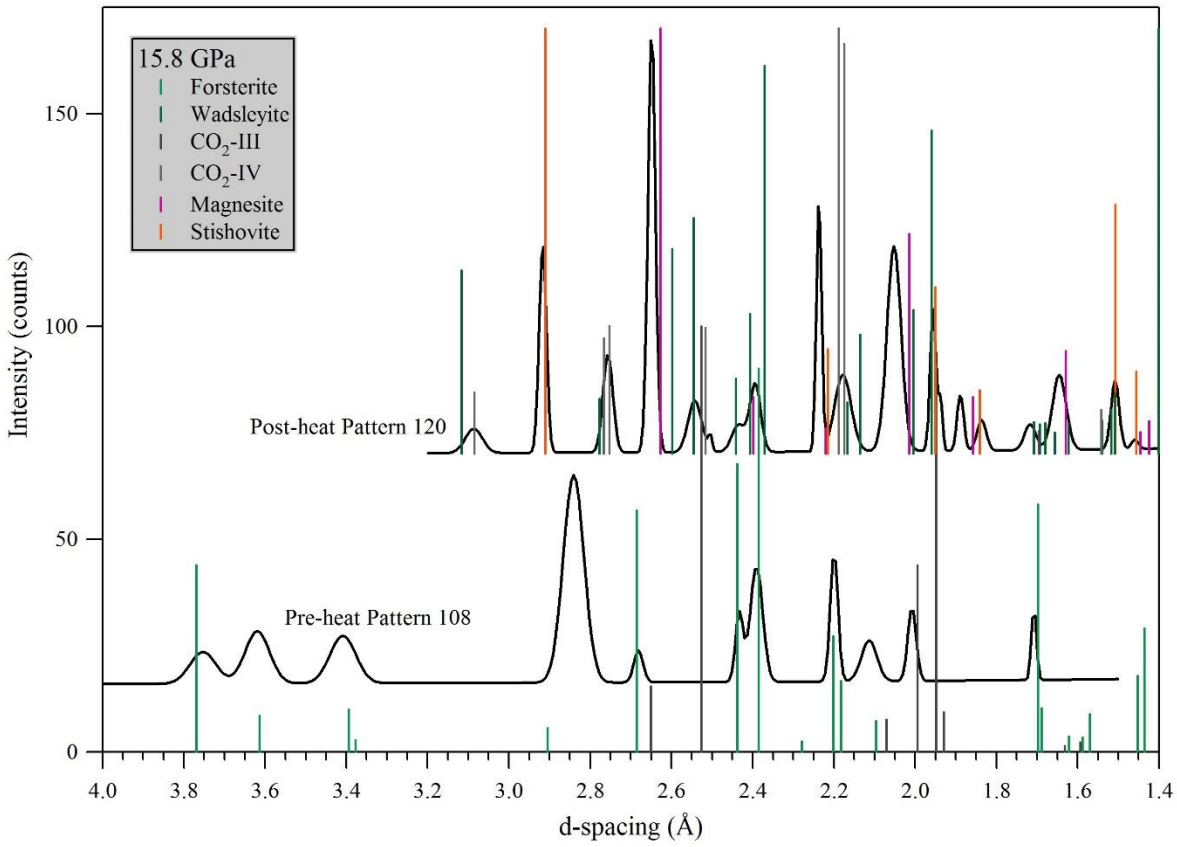

Figure 15. Pre- and post-heated X-ray diffraction patterns at 15.8 GPa. There was growth of CO_2-IV peaks in post-heat pattern 120 as well as Mg_2SiO_4 peaks that represent wadsleyite.

At pressures exceeding 15.8 GPa (Figure 16), magnesite was still seen as a product, with the highest intensity peak of 2.628 Å. Ringwoodite replaced wadsleyite as the observed Mg_2SiO_4 phase. Stishovite was the observed SiO_2 phase in experiments at 21.1 GPa. In post-heat patterns CO_2 was present as both III (1.880 and 2.713 Å) and IV (2.036 and 2.904 Å). There were also a significant number of residual forsterite peaks in the post-heat pattern, specifically at 1.565, 1.695 and 2.372 Å.

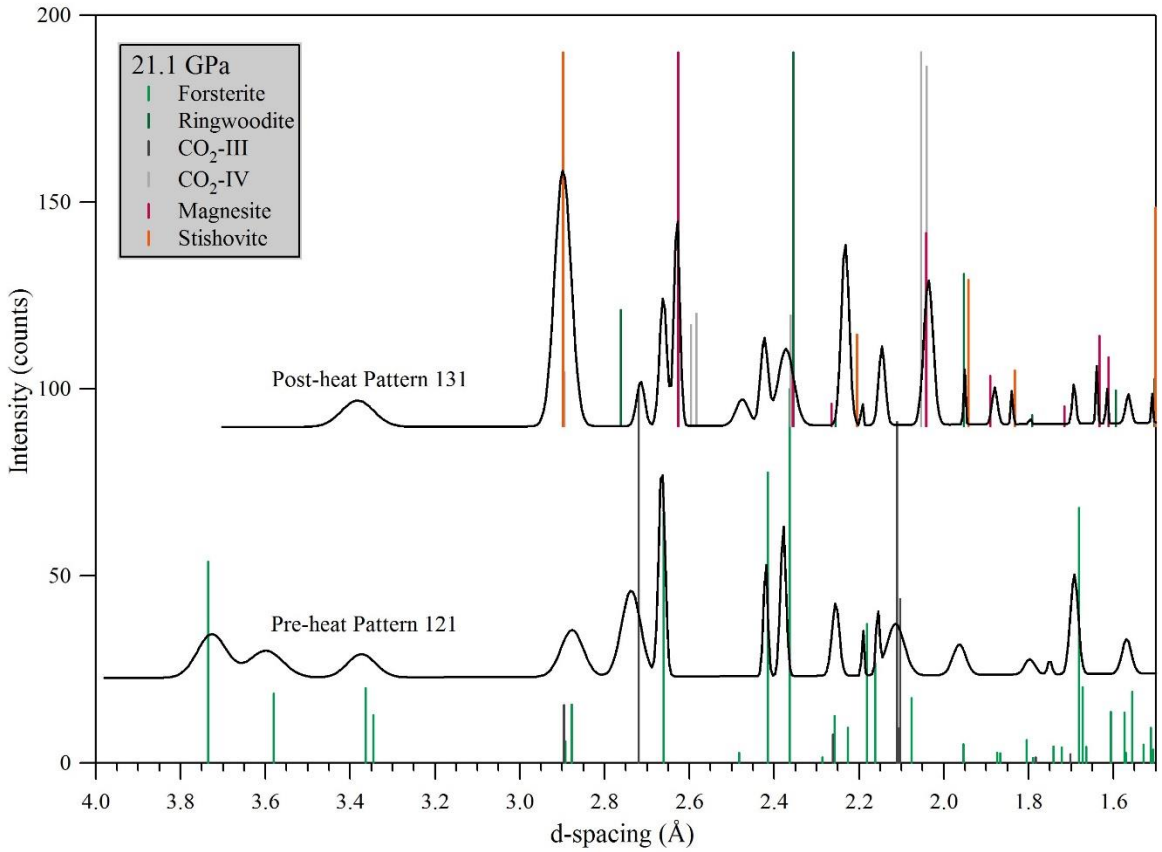

Figure 16. Pre- and post-heated X-ray diffraction patterns at 21.1 GPa. Ringwoodite and stishovite peaks were observed in quench pattern 131. CO_2-IV peaks were observed as well as quenched CO_2-III peaks.

Unit Cell and Volume Trends

The unit cell volumes of the pre- and post-heat phases were calculated from the lattice parameters and are reported in Table 6. Generally, all phase's unit cell volumes decrease with increasing pressure. Additionally, molar volumes are displayed here for convenience as they follow similar trends to unit cell volumes. The specific calculation and importance of the molar volumes are discussed in a later section of this thesis as they were necessary for an easier determination of thermodynamic parameters (e.g. change in volume of the reaction and the Gibbs free energy of reaction). Forsterite pre-heat unit cell volumes decrease consistently with increasing pressure. This is illustrated in Table 6 by a relatively small decrease in volume from 285.9 to 259.1 $Å^3$ with a pressure increase from 2.43 GPa to 21.1 GPa. However, there is a significant increase in the calculated unit cell volume (abc) of 310.2 $Å^3$ at 9.0 GPa which is greater than expected, even considering the significant uncertainty (± 33.2 $Å^3$).

Unit cell volumes for CO_2 changed drastically amongst the solid phases. Pre-heat volumes calculated for CO_2-I consistently decreased from 155.8 $Å^3$ at 2.43 GPa to 123.6 $Å^3$ at 11.7 GPa. Additionally, there is a volume drop to 111.7 $Å^3$ at 21.1 GPa in pre-heat experiments as CO_2 changes phases from I to III. Post-heat CO_2-IV has a strikingly large unit cell volume that decreases from 987.3 to 588.0 $Å^3$ with a pressure change from 15.8 to 21.1 GPa. It is important to note that the molar volumes calculated from such a large unit cell are still comparable to the other phases in this reaction. This is because CO_2-IV has such a large Z value.

Table 6. Pre- and Post-Heat Unit Cell and Volume Data

Pattern	P (Gpa)	Phase	a (Å)	b (Å)	c (Å)	Cell Volume ($Å^3$)	Molar Volume (cm^3/mol)
008	Pre: 0.43	Forsterite	4.75 ± 0.007	10.21 ± 0.017	5.99 ± 0.008	291.1 ± 0.74	43.83
017	Post: 0.48	Forsterite	4.76 ± 0.082	10.24 ± 0.142	5.94 ± 0.089	289.5 ± 0.78	43.58
018	Pre: 2.43	Forsterite	4.73 ± 0.006	10.14 ± 0.009	5.96 ± 0.006	285.9 ± 0.5	43.05
		CO_2-I	5.38 ± 0.004	5.38 ± 0.004	5.38 ± 0.004	155.8 ± 0.4	23.46
049	Post: 1.80	Magnesite	4.62 ± 0.01	4.62 ± 0.01	14.95 ± 0.032	276.1 ± 1.3	27.71
		Orthoenstatite	17.96	9.48	4.69	799.2	30.08
		Quartz	4.84 ± 0.593	4.84 ± 0.593	4.84 ± 1.178	98.3 ± 33.9	19.73
		Forsterite	4.77	10.3	5.86	286.4	43.12
060	Pre: 6.1	Forsterite	4.54 ± 0.383	10.13 ± 0.723	5.94 ± 0.629	273 ± 41.8	41.10
		CO_2-I	5.21	5.21	5.21	141.6	21.32
075	Post: 6.4	Magnesite	4.61 ± 0.014	4.61 ± 0.014	14.73 ± 0.034	271.2 ± 1.8	27.21
		Orthoenstatite	17.96 ± 0.094	8.94 ± 0.232	4.94 ± 0.157	793.5 ± 32.8	29.86
		Coesite	-	-		608.0*	22.89
		Forsterite	4.72	10.8	5.83	297.9	44.85
083	Pre: 9.0	Forsterite	5.43 ± 0.356	9.28 ± 0.58	6.15 ± 0.35	310.2 ± 33.2	46.71
		CO_2-I	-	-	-	132.3	19.91
091	Post: 9.0	Magnesite	4.52 ± 0.018	4.52 ± 0.018	14.7 ± 0.061	259.7 ± 2.3	26.06
		Clinoenstatite	-	-	-	437.4**	65.85
		Coesite	-	-		522.6*	19.67
094	Pre: 11.7	Forsterite	4.66 ± 0.007	9.91 ± 0.014	5.86 ± 0.008	270.5 ± 0.7	40.73
		CO_2-I	4.98 ± 0.011	4.98 ± 0.011	4.98 ± 0.011	123.6 ± 0.8	18.61
104	Post: 11.1	Magnesite	4.53 ± 0.012	4.53 ± 0.012	14.55 ± 0.051	258.1 ± 1.6	25.91
		Clinoenstatite	-	-	-	427.0**	64.28
		Stishovite	4.14 ± 0.003	4.14 ± 0.003	2.64 ± 0.056	45.20 ± 0.1	13.61
108	Pre: 15.4	Forsterite	4.68 ± 0.029	9.91 ± 0.053	5.73 ± 0.031	265.7 ± 2.6	40.00
		CO_2-III	-	-	-	-	-
120	Post: 15.8	Magnesite	4.52 ± 0.01	4.52 ± 0.01	14.38 ± 0.036	254.4 ± 1.3	25.53
		Wadsleyite	5.72 ± 0.112	10.9 ± 0.514	7.95 ± 0.254	495.4 ± 29.9	37.29
		Stishovite	4.12 ± 0.008	4.12 ± 0	2.66 ± 0.011	45.10 ± 0.3	13.59
		CO_2-III	-	-	-	-	-
		CO_2-IV	8.14	8.14	17.19	987.3	24.77
121	Pre: 21.1	Forsterite	4.63 ± 0.076	9.8 ± 0.121	5.72 ± 0.063	259.1 ± 6	39.01
		CO_2-III	4.30	4.51	5.76	111.7	16.81
131	Post: 21.1	Magnesite	4.47 ± 0.702	4.47 ± 0.702	13.86 ± 3.528	239.8 ± 97	24.07
		Ringwoodite	7.4 ± 0.539	7.4 ± 0.539	7.4 ± 0.539	405.9 ± 88.6	30.55
		Stishovite	4.1 ± 0.005	4.1 ± 0.005	2.66 ± 0.007	44.80 ± 0.2	13.48
		Forsterite	4.63 ± 0.021	9.74 ± 0.032	5.76 ± 0.017	260.1 ± 1.6	39.16
		CO_2-IV	8.14	8.14	10.2	588.0	14.75

*** Pressures are taken from ruby fluorescence measurements.**
(-) = Too few XRD peaks to determine using lattice parameters unit cell calculation.
(*) = Supplemental data from Levien and Prewitt, 1981.
(**) = Supplemental data from Shinmei et al., 1999.

Post-heat phases also decrease in volume with increasing pressure. Magnesite's unit cell volume changes by less than 15% from 1.80 to 21.1 GPa (Table 5). $Mg_2Si_2O_6$ as orthoenstatite has a negligible change in volume from 2.43 to 6.1 GPa. Unit cell parameters were not able to be calculated for $Mg_2Si_2O_6$ at 9.0 and 11.1 GPa due to the complexities of the monoclinic crystal system and a lack of high intensity XRD peaks, however, previous data suggest a significant volume drop with a phase change from orthoenstatite to clinoenstatite. Shinmei et al. (1999) suggested a unit cell volume of 437.4 $Å^3$ at 9.1 GPa and 427.0 $Å^3$ at 11.1 GPa. Additionally, there is a fluctuation in the unit cell volume of SiO_2 as it undergoes phase changes throughout the duration of the experiments. Quartz has a unit cell volume of 98.3 $Å^3$ at 2.43 GPa, while coesite (not calculated from this study) has a very large unit cell volume of 608.0 $Å^3$ at 6.4 GPa (Levien and Prewitt, 1981). Stishovite is the stable SiO_2 phase beginning at 11.1 GPa, and has a negligible decrease in volume by less than half of a cubic Angstrom from 11.1 to 21.1 GPa. At experiments at 15.8 GPa wadsleyite is observed with a measured volume of 495.4 $Å^3$. A drop in volume to 405.9 $Å^3$ at 21.1 GPa marks a phase change to ringwoodite.

Whereas the molar volumes of all phases were used for all thermodynamic calculations. the calculated unit cell volumes were used for the identification of structural changes in polymorphs. Furthermore, the stacking arrangement of atoms in one phase are commonly different than other phases, meaning that unit cell volumes are not always directly comparable to another phase. Thus, molar volumes are needed to accurately determine the number of atoms packed into the unit cell by using the Z number associated with a given phase, which accounts for the number of repeating atoms in a unit cell.

Anisotropic Compression of Magnesite

The unit cell volume of magnesite decreases with increasing pressure. This decrease in volume from 276.1 to 239.8 $Å^3$ at pressures ranging from 1.8 to 21.1 GPa is associated with an anisotropic decrease in the unit cell parameters. In a trigonal/hexagonal crystal system, unit cell lengths a=b≠c. The parameters decreased with pressure as expected, however, the c-axis was more compressible than the a-axis (Figure 17). Compression in the c-axis was consistent with the study of Fiquet et al. (2002) and helps to show that magnesite remains in the rhombohedral (trigonal) crystal system from atmospheric pressures up to 21.1 GPa.

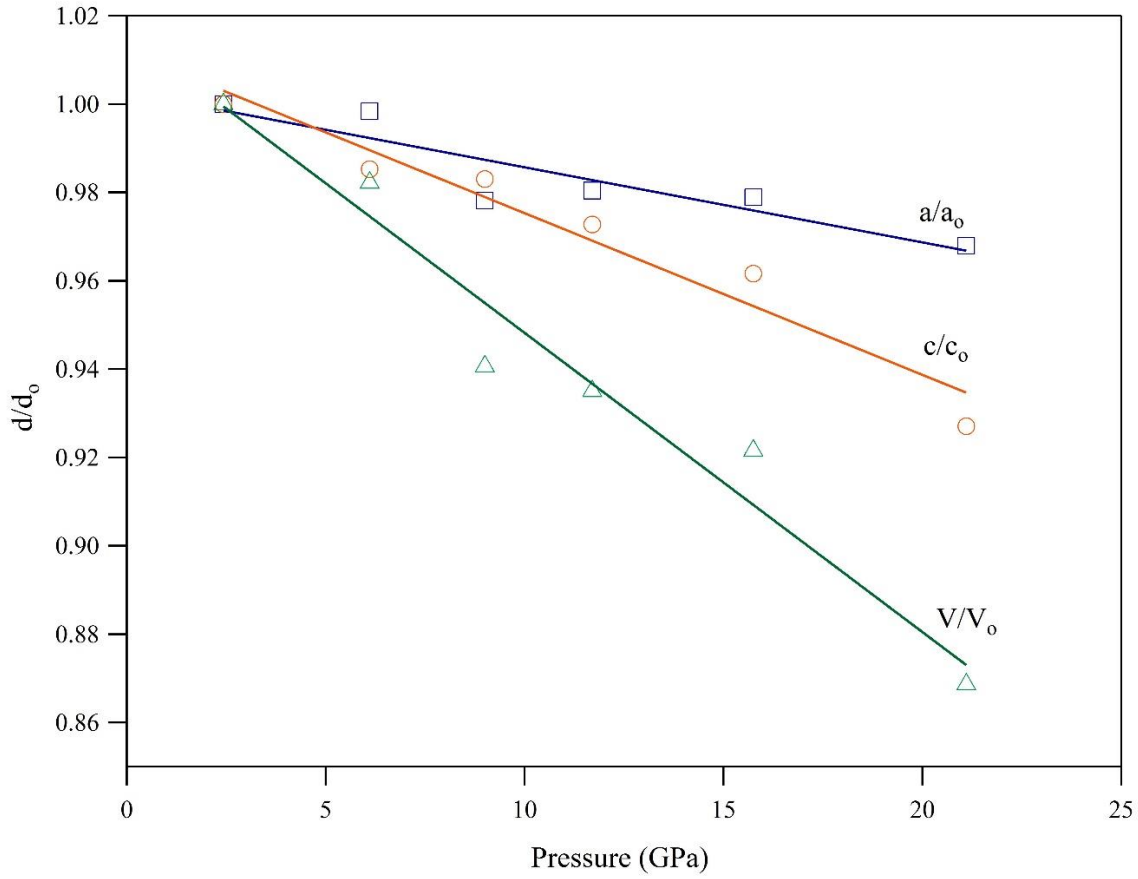

Figure 17. The variation in the unit cell parameters a/a_0 and c/c_0 of magnesite with increasing pressure, where a_0 and c_0 represent the unit cell parameters a and c at atmospheric pressure. Also plotted is the volume with increasing pressure over the initial volume of magnesite. These data were fit with linear trends showing a negative slope.

CHAPTER IV

DISCUSSION

It is accepted that carbon enters the mantle at subduction zones and that not all of the carbon is degassed through volcanism, thus, carbon-bearing phases must exist within the Earth (Alt et al., 2012; Berg, 1986; Dasgupta et al., 2004; Dasgupta et al., 2010). Experimental studies suggest magnesite is stable at temperatures far exceeding the Earth's geotherm, whereas, most other carbonates undergo decarbonation reactions at or above the Earth's geotherm (Fiquet et al., 2002). However, few studies have provided a forward reaction that would support the assumption of present-day magnesite formation in the mantle, making it an important factor in deep carbon storage and cycling (Koziol and Newton, 1998; Fiquet et al., 2002). This study has shown that magnesite can be produced from the reaction of CO_2 and forsterite at pressures and temperatures where the decarbonation of less stable carbonates can release CO_2 and react with mantle phases. Furthermore, the eventual breakdown of magnesite and release of a carbon bearing volatile (e.g. CO_2) at conditions representative of the D" of the core-mantle boundary suggest magnesite may be an important source of carbon necessary for the generation of a HIMU (deep seeded primordial source) magma, carbonatite melt generation, and kimberlite formation within the crust (Collerson et al., 2010).

An earlier study by Koziol and Newton (1998) demonstrated experimentally that magnesite could form from CO_2 and forsterite at high temperatures and pressures up to 3 GPa. Experiments from this study at 2.43 to 11.7 GPa fall within the $MgCO_3 + Mg_2Si_2O_6$ phase

fields, as projected from an earlier study. However, a discrepancy exists between this study and that of Koziol and Newton (1998) in that SiO_2 phases were observed in this study at roughly the same conditions (pressures less than 3.0 GPa). This discrepancy may be a result of their quench style experiments not capturing the equilibrium phase assemblage or due to their relative low CO_2 fugacity in the experimental charge. The addition of the SiO_2 phase would change the slope of the equilibrium curve, however the experiments would still fall within the magnesite stability field as expected.

The presence of only magnesite and stishovite as run products at pressures greater than 11.7 GPa suggests the reaction of Koziol and Newton (1998), which notes $Mg_2Si_2O_6$ as a reaction product, may only be supported at less than 3 GPa. The lack of $Mg_2Si_2O_6$ at high pressures demonstrates a likely equilibrium boundary between 11.7 and 15.8 GPa (Figure 18). This study has increased the range of magnesite stability defined by a forward reaction as well as identify *in-situ* phase changes and products not seen in the Koziol and Newton (1998) study and, therefore, will allow for a more thorough characterization of carbon reactivity in the mantle.

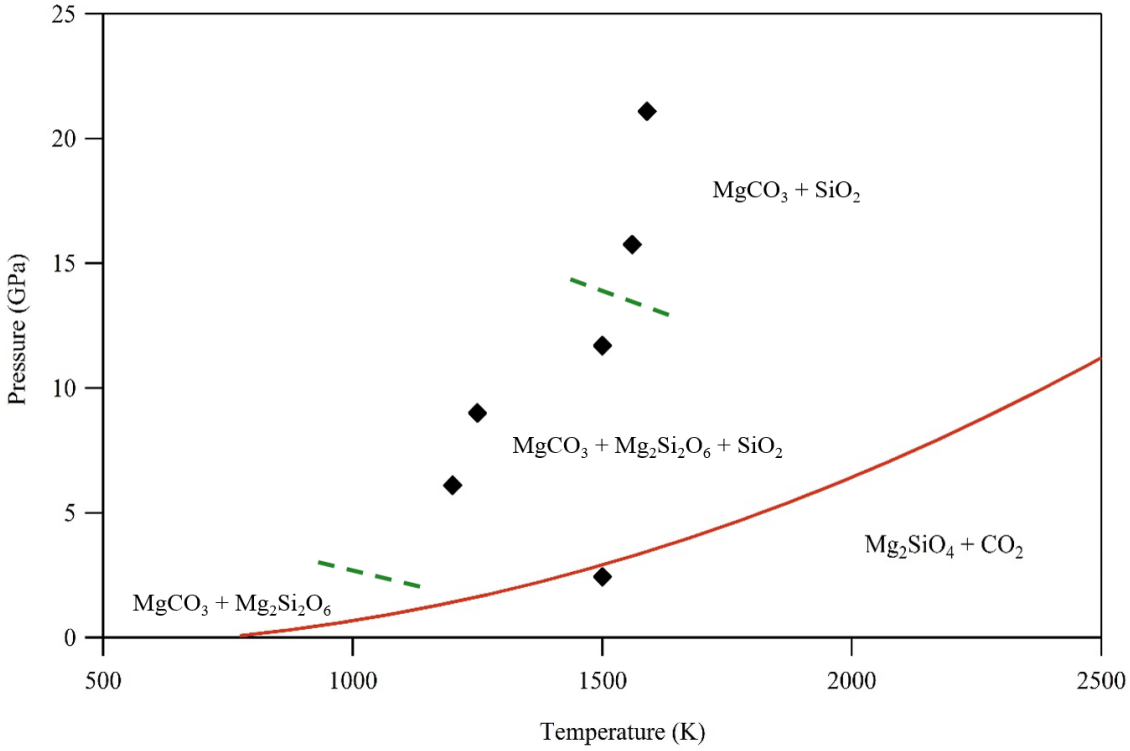

Figure 18. Pressure vs Temperature plot showing the equilibrium boundary between forsterite + CO_2 and magnesite + enstatite from Koziol and Newton, 1998. An additional boundary is schematically placed at higher pressures to simulate the lack of enstatite at these conditions. This equilibrium boundary has been extended to higher pressures to better represent the data.

Hypothesized Magnesite-Forming Reactions

The presence of magnesite is clearly shown in all post-heat XRD patterns at pressures greater than 1.0 GPa. Magnesite is a reaction product that is stable for the entire range of pressure and temperature conditions of this study. $Mg_2Si_2O_6$ (enstatite) and SiO_2 (quartz or coesite) were observed in all experiments conducted at $P < 11.7$ GPa. Run products from experiments conducted at $P \geq 11.7$ included only $MgCO_3$ (magnesite) and SiO_2 (stishovite).

Therefore, reactions 1 and 2 represent the observed phases at pressures below and above 11.7 GPa, respectively.

$$2Mg_2SiO_4 + 3CO_2 = 3MgCO_3 + \frac{1}{2}Mg_2Si_2O_6 + SiO_2 \quad (1)$$

$$Mg_2SiO_4 + 2CO_2 = 2MgCO_3 + SiO_2 \quad (2)$$

The absence of enstatite in reaction 2 allows for more moles of magnesite to be produced relative to the reactant forsterite due to the magnesium not being locked up in enstatite. $Mg_2Si_2O_6$ changes phase from ortho to clinoenstatite from 2.43 GPa to 11.7 GPa and is not stable at pressures greater than ~15 GPa (Fei and Bertka, 1999). The data from this study support that contention as enstatite is not present in experiments at P < 15 GPa. Additionally, Mg_2SiO_4 exists as forsterite until 11.7 GPa and transitions into wadsleyite at 15 GPa and ringwoodite at 21 GPa at elevated temperatures (Figure 19). Reactions 1 and 2 provide possible processes for magnesite formation at elevated temperatures from a range of the upper mantle to the transition zone. The thermodynamics of these equations further constrain magnesite stability and how it relates to changes in volume, pertaining to both unit cell and phase changes as well as how this effects the Gibbs free energy of reaction, and how these factors control the fate of the reaction and hence magnesite production.

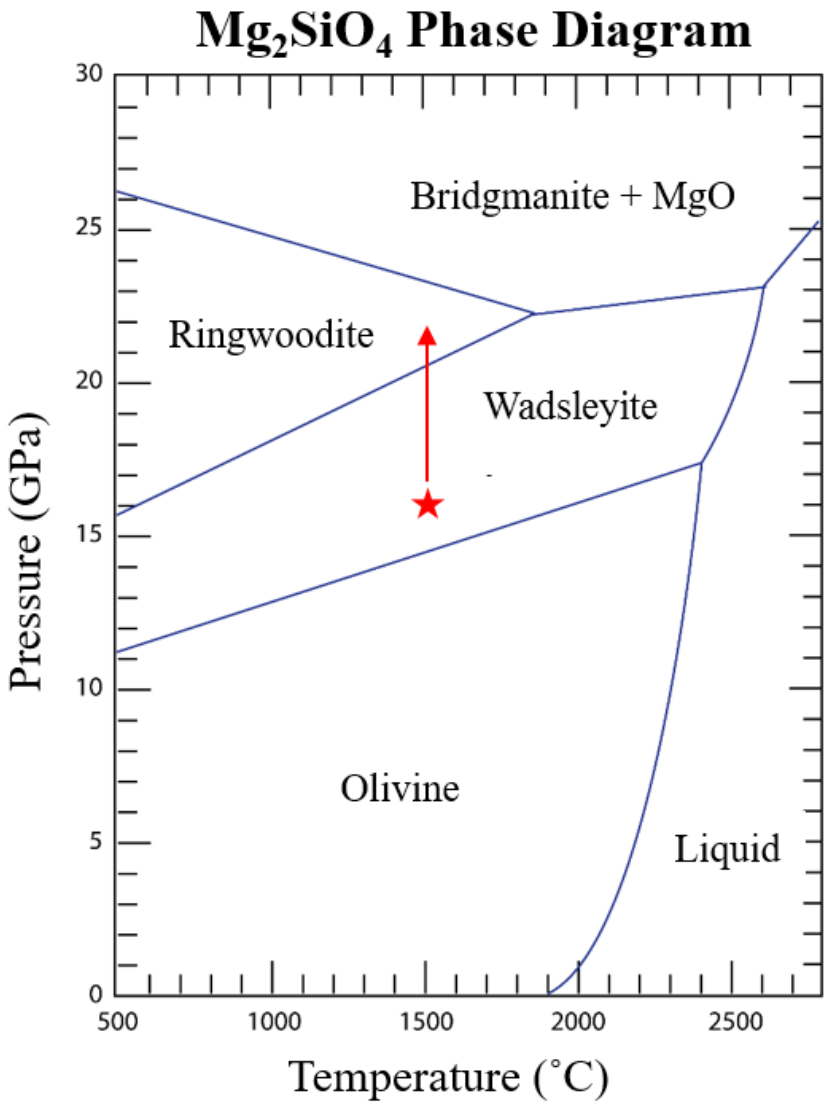

Figure 19. Mg_2SiO_4 Phase Diagram showing experimental conditions from this study. Modified from Fei and Bertka, 1999. Mg_2SiO_4 changes phase from forsterite (at pre-heat conditions) to wadsleyite then ringwoodite with increasing pressure and temperature.

Thermodynamic Modeling - Volumes of Reaction

Reaction 1 has been used to calculate the molar change in volume and Gibbs free energy of the reaction from 2.43 to 11.7 GPa and Reaction 2 is used at 15.8 and 21.1 GPa. The unit cell volumes, V_{cell}, calculated in the results section were used to calculate molar volumes by using the following relationship:

$$V_{molar} = \frac{N_A V_{cell}}{Z} \quad (3)$$

where N_A is Avogadro's number, Z is the number of formula units in the unit cell, and V_{cell} is in cm^3/mol. The molar volume allows for the comparison of volumes between phases, which allows for the change in volume of the reaction (ΔV_{rxn}) to be calculated. These calculations were done at both high temperature and at quench temperature.

The ΔV_{rxn} value is calculated by subtracting the total volume of the reactants from the total volume of the products and is often negative or near zero for reactions at elevated pressure as large positive values would indicate a reaction that undergoes volumetric expansion which is usually only sustainable if there is a correspondingly large negative enthalpy term. The change in the molar volume of the reaction (ΔV_{rxn}) was calculated based on the phases identified in the XRD patterns in the molar proportions outlined in Reactions 1 and 2 and plotted as a function of pressure (Figure 20). ΔV_{rxn} increases with increasing pressure until the products begin to have a larger volume than the reactants at > 8 GPa. This trend is seen from 2 to 11 GPa, where the volume of the products is increasing mainly due to the transition of $Mg_2Si_2O_6$ from orthoenstatite to clinoenstatite. This structural change from orthorhombic to monoclinic is equivalent to a total volume of reaction increase of 29.9 to 65.9

cm^3/mol, which shifted the ΔV_{rxn} from negative to positive, inhibiting magnesite formation. If this reaction was driven by these changes in volume alone, then magnesite production would not be observed, however, magnesite was observed at all experimental pressures, regardless of the volume constraints. Therefore, this study indicates the enthalpy and entropy terms may be the driver of this reaction in favor of magnesite production (Scott et al., 2013).

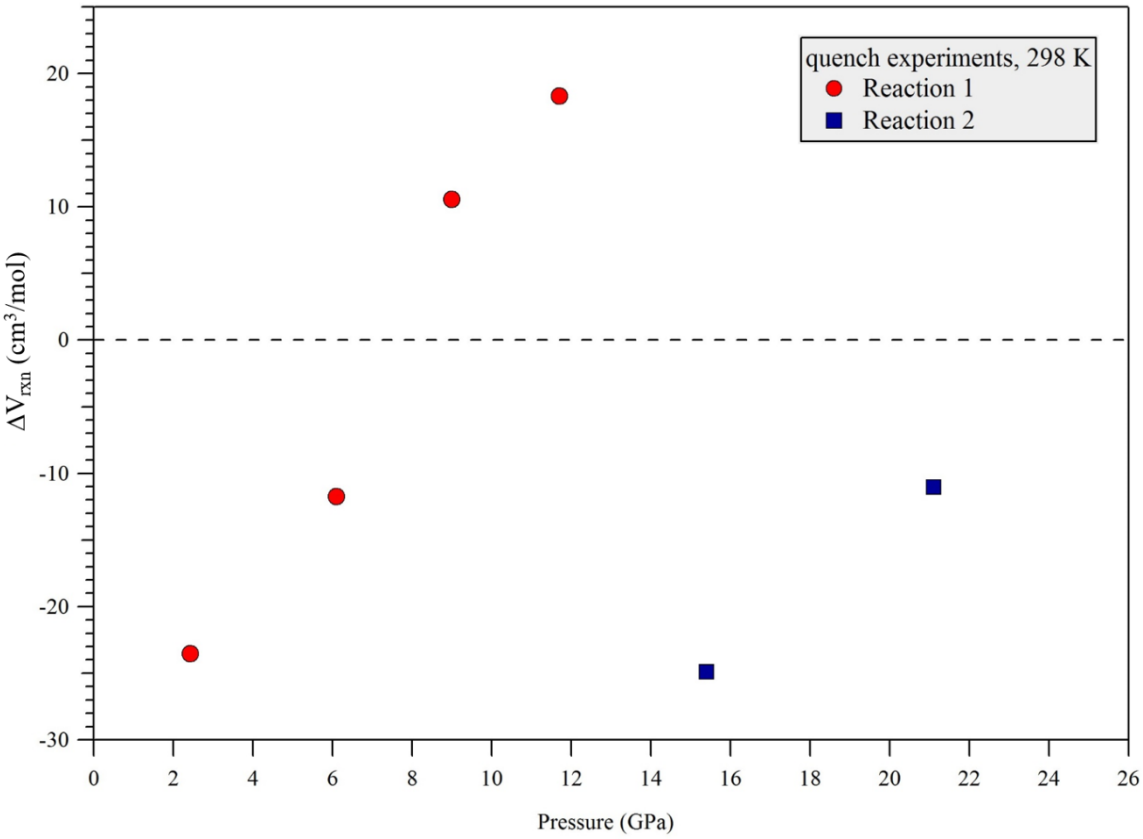

Figure 20. Change in molar volume of the reaction (ΔV_{rxn}) with pressure after quench. The molar volumes were determined from the unit cell volumes of each phase. ΔV_{rxn} was determined by using Reaction 1 from 2 to 11 GPa and Reaction 2 from 15 to 21 GPa.

There is a drop in the volume from 11 to 15 GPa that is associated with phase changes of CO_2 and the non-production of $Mg2Si2O_6$. A structural change from cubic CO_2-I to hexagonal CO_2-IV was observed at these conditions. It is also important to note that CO_2-III was observed as low intensity peaks in XRD patterns, however, no volume data was able to be calculated for this phase, which is explained in the methods section of this study. The absence of $Mg_2Si_2O_6$ (Fei and Bertka, 1999) in the run products at $P \geq 15$ GPa required that its volume be removed from the equation, and molar proportions of other phases shifted following Reaction 2. This is the primary reason for the calculated decrease in the ΔV_{rxn}.

Mg_2SiO_4 exists as wadsleyite from approximately 13-18 GPa and ringwoodite from 18-24 GPa. SiO_2 is present as coesite and stishovite at pressures of approximately 2.5-9 GPa and > 9 GPa, respectively. At high pressures the transition of forsterite to denser Mg_2SiO_4 phases may slow magnesite growth, however, the lack of $Mg2Si2O_6$ likely drives the reaction towards the products, thus favoring the production of magnesite, due to the decrease in ΔV_{rxn}. At low temperatures, volumetric effects may be a very important driver for this reaction. At high temperatures (1500 K) the volume term is two orders of magnitude more negative because CO_2 is present as a fluid, causing an overwhelming negative volume term, however, at pressures higher than 40 GPa at 1500 K, CO_2-IV is stable (Scott et al., 2013) which would increase the $\Delta V_{rxn,}$ term and may slow or inhibit magnesite formation. Since there are still products observed, despite a ΔV_{rxn} that prefers the reactants, the enthalpy term (unknown at these conditions) is thought to control the reaction and drive it towards the products (Scott et al., 2013).

Thermodynamic Modeling - Gibbs Free Energy of Reaction

The Gibbs free energy of the reaction can be used to determine whether the products or the reactants will be the favored assemblage by the following relationship:

$$\Delta G_{rxn} = \Delta H_{rxn} - T\Delta S_{rxn} + (P-1)\Delta V_{rxn} \quad (4)$$

If ΔG is greater than zero the reactants are favored and the reaction will not proceed. If ΔG is less than zero, the products are favored. The phases that produce the smallest free energy are those that are favored in a reaction. The Gibbs free energy equation is useful as a first order approximation for how a reaction will behave with increasing pressure and temperature.

Standard state thermodynamic parameters (ΔH, ΔS) from Robie, Hemingway and Fisher (1979), and parameters experimentally determined from this study (ΔV) were used to provide a first order estimate of the Gibbs free energy of reaction. These values are calculated at room temperature (data used from quench phases) and 1500 K, and used to calculate ΔG_{rxn} for pressures up to 21.1 GPa.

The ΔG_{rxn} calculated at high temperature (1500K) becomes increasingly negative as pressure increases for Reactions 1 and 2 (Figure 21). Fluid CO_2 values (Robie, Hemingway, and Fischer, 1979) dominate the Gibbs free energy equation, and such large reactant volumes rapidly drive the reaction toward the products (negative ΔG_{rxn} values). The results from this study show that Reactions 1 and 2 favor the products at high pressure and temperature because they have a lower Gibbs free energies and much smaller total volumes.

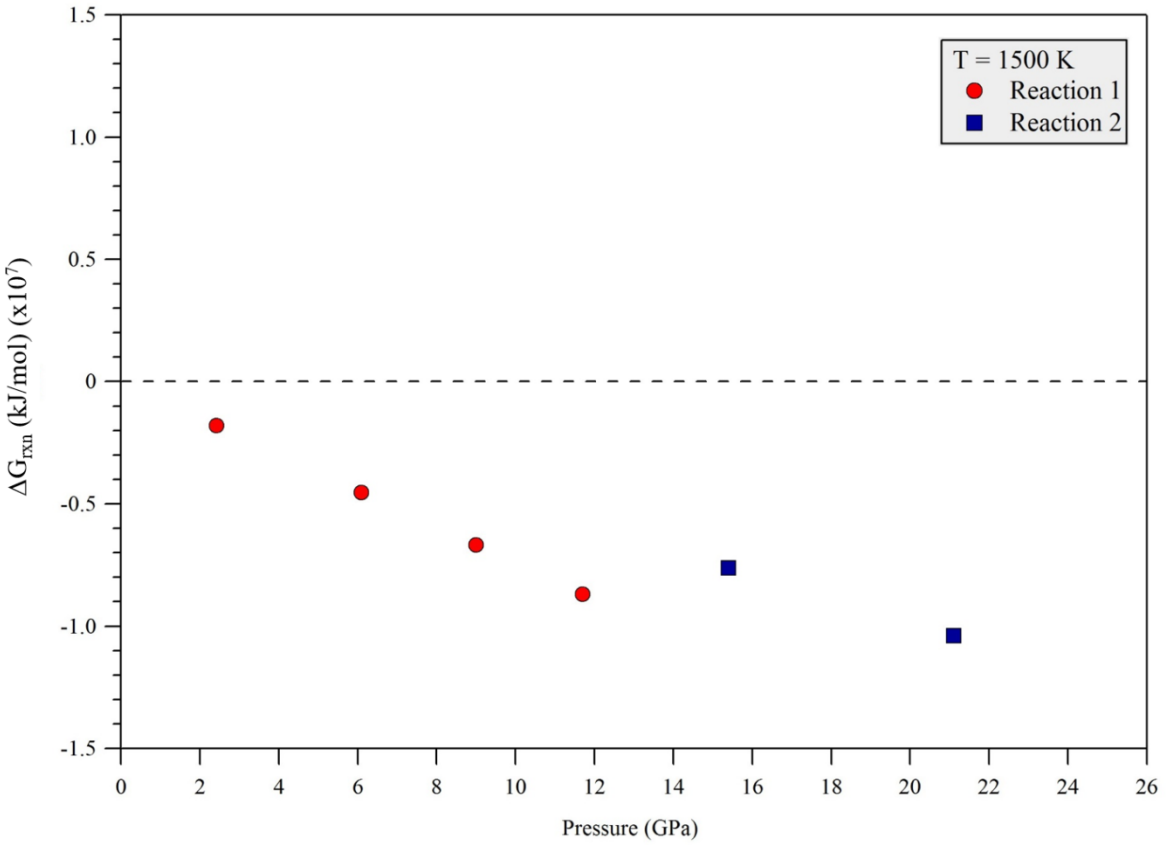

Figure 21. Gibbs free energy of reaction with increasing pressure at 1500 K. Reactions 1 and 2 display decreasing free energy with increasing pressure, suggesting a reaction driven towards magnesite formation.

The Gibbs free energy of the reaction calculated from quenched volumes show a similar trend as the change in volume of the reaction with increasing pressure. The calculation of the Gibbs free energy is entirely dependent on the volume terms, because the enthalpy and entropy of these phases are unknown at these pressures, and hence standard pressures must be used at temperature (Robie, Hemingway, and Fischer, 1979). The lack of thermodynamic data at the relevant conditions of the experiments is not ideal, but it does not preclude a comprehensive analysis of those factors that may be important in controlling the reaction of CO_2 with silicate minerals. Since CO_2 is a solid at these conditions, the volume term may hinder magnesite formation. Considering CO_2 has a stoichiometric coefficient of three in reaction 1, it has significant impact on the volume of reaction. Figure 22 shows that as pressure increases from 2 to 11 GPa, the ΔG_{rxn} goes from negative (products favored) to positive (reactants favored) when modeling with volumes at 298 K. The absence of $Mg_2Si_2O_6$ in the reaction products at 15 GPa results in a drop in the Gibbs free energy, and once again the reaction favors the products. The trend suggests that as pressure increases, the Gibbs free energy will increase, which may limit the formation of magnesite at high pressure, when CO_2 is in the solid phase fields. The calculated ΔG_{rxn} is positive at 21.1 GPa, which suggests that Reaction 2 should favor the reactants, however, magnesite and stishovite were produced. The uncertainty in the CO_2-IV thermodynamic data could be the source of the error, or perhaps a depressed enthalpy term is driving the reaction at 21.1 GPa. Future studies that provide enthalpies and entropies for high pressure mantle phases are required to better constrain the Gibbs free energies of all phases, but most especially CO_2, at these conditions.

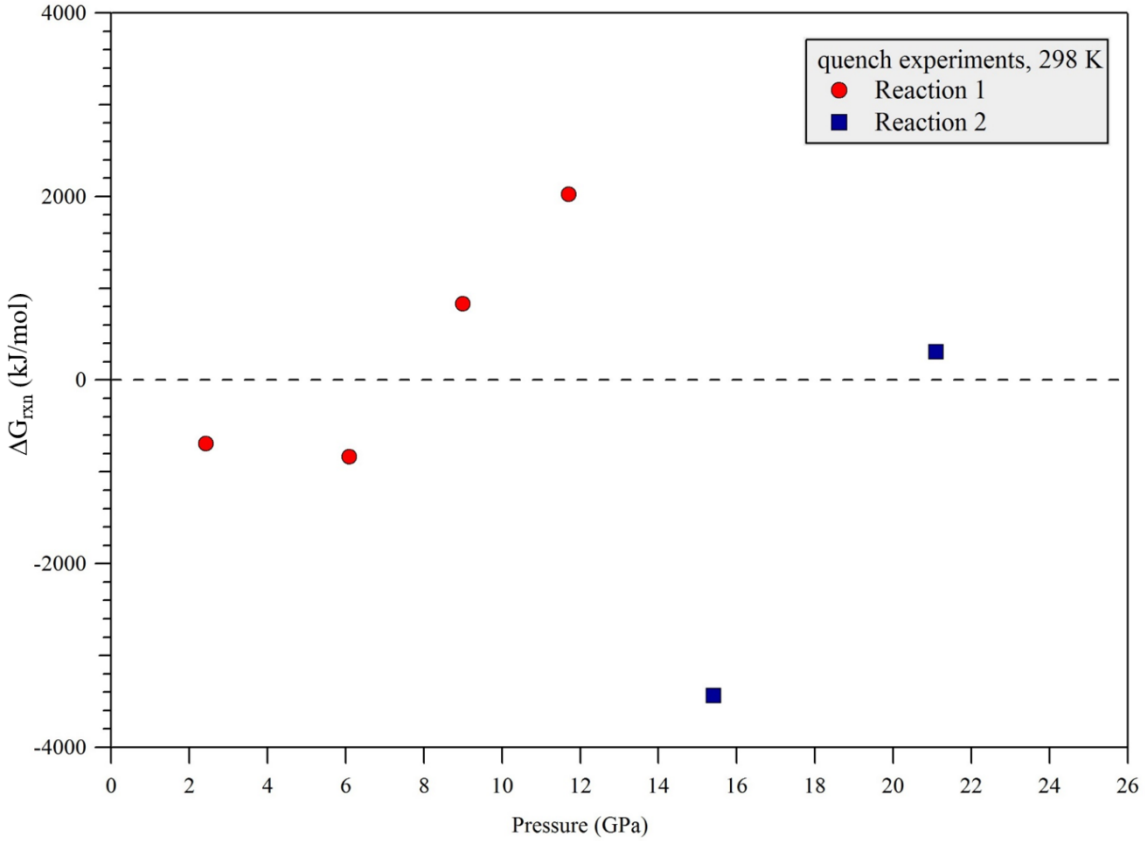

Figure 22. Gibbs free energy of reaction with increasing pressure after quench. Quenched experiments contain solid CO_2. Gibbs free energy calculations at quench conditions show the effects of solid CO_2 on reactions 1 and 2.

Natural Application

This study has shown that under high $f_{CO_2}^{fluid}$ and a_{CO_2} conditions, forsterite and carbon dioxide will react to produce magnesite, enstatite, and quartz at pressures < 15 GPa, and magnesite and stishovite at pressures > 15 GPa. The experiments were conducted at upper mantle and transition zone pressures and temperatures and illustrate that CO_2, produced by the breakdown of unstable carbonates (e.g., calcite, dolomite) during subduction, will react with Mg-bearing silicates and produce a substantial amount of magnesite. Magnesite has been shown to be stable throughout the majority of the Earth's mantle and provides a mechanism through which carbon can be transferred to the lower mantle or even possibly the core-mantle boundary (CMB). Furthermore, evidence from inclusions within transition zone diamonds confirm the existence of carbonate-rich melts in the lower mantle (Kaminsky et al., 2009), which may support both slab propagation to the CMB and/or deep mantle convection of magnesite (Collerson et al., 2010; Kaminsky et al., 2009).

Magnesite has been stated to be stable in the lower mantle until depths of about 300 – 400 km above the CMB (Ishikki et al., 2004). This roughly corresponds to the D'' layer which has been noted in seismic studies to project upward from the CMB (Lay et al., 1998). Experimental extrapolations of the geotherm to these conditions show that the geotherm intersects the magnesite solidus, which would induce a carbon-rich melt. Devolitization of a carbon bearing phase could induce melting at the CMB and is suggested to produce a carbon-rich (HIMU source – A melt with a high $^{238}U/^{204}Pb$ ratio from a primordial source AKA virgin melt) plume that rises from the CMB due to its high buoyancy (Collerson et al., 2010). After melt generation this plume rises as a mechanically separate solid due to density

differences between the carbon-rich silicate plume and the silicate lower mantle. It is not well constrained how much these solid plumes interact with the mantle as they ascend through it, and if volatiles are lost or added as this is speculative, however, Collerson et al. (2010) has hypothesized that this solid plume could initiate a secondary melt near the transition zone, as the carbon rich silicate again crosses the geotherm. This secondary melt may be especially important in the generation of kimberlites which have both an enriched mantle and a HIMU source (Figure 23). The reactions determined from this study have implications that may serve to drive kimberlite ascension. In a hypothetical reduced environment, carbonate rich kimberlites can release CO_2 by a devolitization reaction that may be the reverse of Reaction 1 and 2 from this study. This process would produce both CO_2 and forsterite giving kimberlites their chemical signature, and also provide continual flux melting by continuously introducing a carbon-volatile to the melt leading to an explosive eruption (Russell et al., 2012). It may also be plausible that decarbonation reactions are occurring at the transition zone and may provide the carbon necessary for diamond formation.

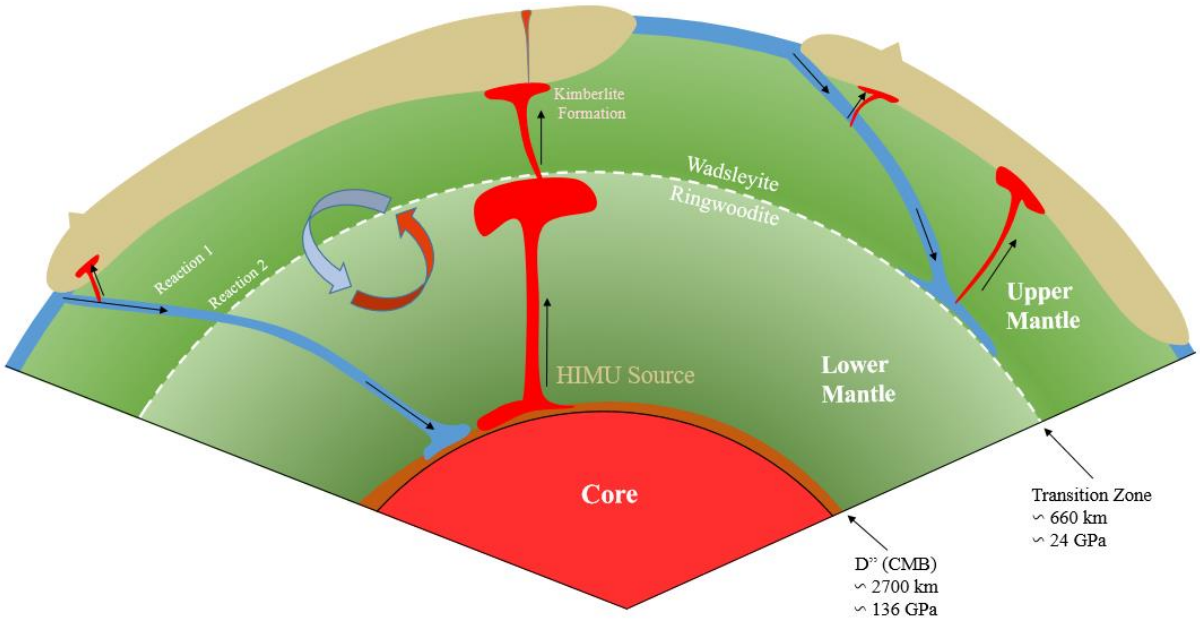

Figure 23. Schematic of the Earth illustrating deep carbon cycling. This figure demonstrates the subduction of carbonates, the release of CO_2 by decarbonation reactions, the formation of magnesite by Reactions 1 and 2, the transfer of magnesite to the CMB, generation and ascension of a plume and kimberlite formation which returns CO_2 to surface reservoirs. Schematic is not to scale.

Future Work

Fiquet et al. (2002) showed that magnesite would not breakdown at high pressures and temperatures, however, they did not address whether it could form from CO_2 and more common mineral phases within the mantle. Scott et al. (2013) illustrated, for the first time, that magnesite could form from the reaction of CO_2 with MgO (periclase). They also noted the production of magnesite may be limited by volumetric constraints at the pressures of the transition zone and lower mantle. The purpose of this study was to add a more realistic component to the Scott et al. (2013) study by introducing Mg_2SiO_4 as a reactant, rather than

MgO. There is an agreement between this study and Scott et al. (2013) as both conclude that magnesite can form in the mantle and that there is an increase in the ΔV_{rxn} with increasing pressure.

In order to better approximate natural conditions a future project should consider the reactivity of CO_2 with solid solution minerals including olivine and pyroxene. In this case, activities of all phases would need to be constrained, however, the resulting mineral phases might provide further insight into carbon storage. Solid solution Mg-Fe carbonate (ferro-magnesite) may be produced at lower mantle depths > 1800 km (Liu et al., 2015). If this is the case, Mg and Fe in the lower mantle may be locked away in carbonates and less available to perovskites. Mg and Fe in the perovskite structure allows large spaces for OH^- groups (Murakami et al., 2002; Nestola and Smith, 2015), so a decrease in the amount of magnesium and iron available to perovskites could mean potentially less water storage in the mantle, however it may increase the amount of C being held in the mantle. Additionally, DAC studies that take CO_2 to high pressure will be important for gathering high pressure data for this phase including volume and atomic structures of the several CO_2 phases. This will be important for identifying how these high density volatile phases may react in the lower mantle and be used to better constrain the high pressure CO_2 phase diagram as well as carbon reactivity in the deep mantle.

CHAPTER V

CONCLUSION

The exchange of carbon between the Earth's interior and its surface has important petrologic and atmospheric implications, however, there is a dearth of data on carbon's reactivity at pressures and temperatures that correspond to the deep Earth. This study evaluated the reactivity of CO_2 with common mantle phases at pressures and temperatures up to 21 GPa and 1500 K, respectively. The experiments were conducted by using diamond anvil cells (DACs) and *in situ* X-ray diffraction measurements of all solid phases present. The reactivity of CO_2 with silicate minerals could be measured by analyzing pre- and post-heating experiment of reactants and run products. The data obtained demonstrated that magnesite formed at pressures from 2.43 to 21.1 GPa through the reaction of CO_2 and Mg_2SiO_4. Thus, magnesite is stable within the Earth's upper mantle and transition zone and may extend into the lower mantle and serve as a reservoir for deep carbon.

The observed run products, other than magnesite, varied as a function of pressure and temperature. Previous studies have shown the production of magnesite and enstatite at pressures of ~ 2 GPa (Koziol and Newton, 1998) whereas this study extended the pressure and temperatures range up to 21.1 GPa. This study confirmed the run products (magnesite and enstatite) observed by Koziol and Newton (1998) at pressures < 3 GPa, but also noted a SiO_2 phase from 2.43 to 11.7 GPa and the loss of enstatite as a product from 15.8 to 21.1 GPa. Several phase changes were also noted in both reactants and products in the higher pressure

experiments of this study. All pre-heat peaks are observed as forsterite, however, post-heat wadsleyite and ringwoodite peaks are observed at 15.8 and 21.1 GPa, respectively. Pre-heat CO_2 is observed as a gas at room pressure and temperature and changes phase from fluid to solid as the sample is pressurized and/or the temperature is lowered. As temperature decreases, CO_2 falls from the fluid field into solid carbon dioxide phases in P-T space. These carbon dioxide phases include CO_2-I at 2.43 and 6.1 GPa (pre-heat), CO_2-III (post-heat) up to 21.1 GPa, and CO_2-IV observed at 21.1 GPa. Magnesite did not change structure throughout this study, however, the c-axis was shortened nearly 2x as much as the a and b axes, which is consistent with previous studies documenting magnesite compressibility with pressure (Fiquet et al., 2002; Scott et al., 2013). SiO_2 was present from 2.43 to 21.1 GPa and changed from quartz to stishovite, though the total molar volume change for SiO_2 is minimal. Enstatite ($Mg_2Si_2O_6$) undergoes structural changes relating to pressure from ortho to clinoenstatite at 9 GPa. The loss of $Mg_2Si_2O_6$ at 15.8 GPa causes a significant drop in ΔV_{rxn} which in turn lowered the ΔG_{rxn}, making the production of magnesite more preferred. Some thermodynamic modeling predicts a slightly positive ΔG_{rxn} at 11.7 and 21.1 GPa (e.g. Figure 22), suggesting no magnesite formation, however, distinct magnesite XRD peaks are visible at all pressures. This suggests that either the enthalpic energy is dominant or that the enthalpies and entropies of these high-pressure phases need to be better constrained.

Magnesite stability in the upper mantle and transition zone has been documented by several studies. Reactions 1 and 2 from this study support those previous works while additionally providing a mechanism for magnesite formation in subducting slabs that are penetrating beyond arc depths where CO_2 is being released by decarbonation reactions (i.e. calcite, dolomite). This study and other experimental studies support the stability of magnesite

and other select carbonates within the upper mantle and transition zone; further, the presence of carbonate inclusions in diamonds provides verification in natural samples (Berg, 1986; Brenker et al., 2007). Magnesite has been shown to resist break down in DAC studies up to 115 GPa and temperatures of 1500 K and has been shown to form through the reaction of CO_2 with MgO (up to 40 GPa, Scott et al., 2013) and Mg_2SiO_4 (up to 21.1 GPa, this study). Magnesite may be transferred into the lower mantle by mantle convection or deep slab propagation where the release of a carbon volatile induces melting that may be associated with the formation of HIMU and/or carbonatite melts accounting for chemical heterogeneities in the mantle. Additionally, if magnesite is an accessory mineral in the mantle, it may be important in the formation of kimberlites by providing volatile-induced ascension through its back reaction with silicate minerals to produce volatile CO_2 (Russell et al., 2012). Magnesite as a potential reservoir for carbon in the mantle provides an explanation for both the projected long term (billions of years) residence time for mantle carbon as well as a means of recycling carbon to surface reservoirs by the generation of deep melts and the eventual degassing of CO_2 or CH_4 at the surface.

REFERENCES

Alt, J.C., Garrido, C.J., Shanks, W.C., Turchyn, A., Padrón-Navarta, J.A., López Sánchez-Vizcaíno, V., Gómez Pugnaire, M.T., and Marchesi, C. (2012) Recycling of water, carbon, and sulfur during subduction of serpentinites: A stable isotope study of Cerro del Almirez, Spain: Earth and Planetary Science Letters, v. 327-328, p. 50–60, doi: 10.1016/j.epsl.2012.01.029.

Angel, R.J., Allan, D.R., Miletich, R., and Finger, L.W. (1997) The use of quartz as an internal pressure standard in high-pressure crystallography: Journal of Applied Crystallography, v. 30, p. 461–466.

Angel, R.J., Alvaro, M., and Gonzalez-Platas, J. (2014) EosFit7c and a Fortran module (library) for equation of state calculations: Zeitschrift für Kristallographie - Crystalline Materials, v. 229, doi: 10.1515/zkri-2013-1711.

Angel, R.J., Chopelas, A., and Ross, N.L. (1992) Stability of high-density clinoenstatite at upper-mantle pressures: Nature, v. 358, p. 322–324, doi: 10.1038/358322a0.

Angel, R.J., and Jackson, J.M. (2002) Elasticity and equation of state of orthoenstatite, MgSiO3: American Mineralogist, v. 87, p. 558–561.

Bailey, D.K. (1980) Volatile flux, geotherms, and the generation of the kimberlite-carbonatite-alkaline magma spectrum: Mineral. Mag, v. 43, p. 695–699.

Berg, G.W. (1986) Evidence for carbonate in the mantle: Nature, v. 324, p. 50–51, doi: 10.1038/324050a0.

Birle, J. D., Grass, G. V., Moore, P. B., and Smith, J. V. (1968) Crystal structures of natural olivines: American Mineralogist, v. 53, p. 807-824.

Boulard, E., Gloter, A., Corgne, A., Antonangeli, D., Auzende, A.-L., Perrillat, J.-P., Guyot, F., and Fiquet, G. (2011) New host for carbon in the deep Earth: Proceedings of the National Academy of Sciences, v. 108, p. 5184–5187.

Brenker, F.E., Vollmer, C., Vincze, L., Vekemans, B., Szymanski, A., Janssens, K., Szaloki, I., Nasdala, L., Joswig, W., and Kaminsky, F. (2007) Carbonates from the lower part of transition zone or even the lower mantle: Earth and Planetary Science Letters, v. 260, p. 1–9, doi: 10.1016/j.epsl.2007.02.038.

Collerson, K.D., Williams, Q., Ewart, A.E., and Murphy, D.T. (2010) Origin of HIMU and EM-1 domains sampled by ocean island basalts, kimberlites and carbonatites: The role of CO2-fluxed lower mantle melting in thermochemical upwellings: Physics of the Earth and Planetary Interiors, v. 181, p. 112–131, doi: 10.1016/j.pepi.2010.05.008.

Dasgupta, R. (2013) Ingassing, Storage, and Outgassing of Terrestrial Carbon through Geologic Time: Reviews in Mineralogy and Geochemistry, v. 75, p. 183–229, doi: 10.2138/rmg.2013.75.7.

Dasgupta, R., and Hirschmann, M.M. (2010) The deep carbon cycle and melting in Earth's interior: Earth and Planetary Science Letters, v. 298, p. 1–13, doi: 10.1016/j.epsl.2010.06.039.

Dasgupta, R., Hirschmann, M.M., and Smith, N.D. (2007) Partial Melting Experiments of Peridotite + CO2 at 3 GPa and Genesis of Alkalic Ocean Island Basalts: Journal of Petrology, v. 48, p. 2093–2124, doi: 10.1093/petrology/egm053.

Dasgupta, R., Hirschmann, M.M., and Withers, A.C. (2004) Deep global cycling of carbon constrained by the solidus of anhydrous, carbonated eclogite under upper mantle conditions: Earth and Planetary Science Letters, v. 227, p. 73–85, doi: 10.1016/j.epsl.2004.08.004.

Datchi, F., Giordano, V.M., Munsch, P., and Saitta, A.M. (2009) Structure of Carbon Dioxide Phase IV: Breakdown of the Intermediate Bonding State Scenario: Physical Review Letters, v. 103, doi: 10.1103/PhysRevLett.103.185701.

Fei, Y., and Bertka, C. M. (1999) Phase transitions in the Earth's mantle and mantle mineralogy, in Mantle Petrology: Field Observations and High Pressure Experimentation: Geochemical Society Special Publications, v. 6, p. 189-207

Fiquet, G., Guyot, F., Kunz, M., Matas, J., Andrault, D., and Hanfland, M. (2002) Structural refinements of magnesite at very high pressure: American Mineralogist, v. 87, p. 1261–1265.

Frost, D.J., and McCammon, C.A. (2008) The Redox State of Earth's Mantle: Annual Review of Earth and Planetary Sciences, v. 36, p. 389–420, doi: 10.1146/annurev.earth.36.031207.124322.

Giordano, V.M., Datchi, F., Gorelli, F.A., and Bini, R. (2010) Equation of state and anharmonicity of carbon dioxide phase I up to 12 GPa and 800 K: The Journal of Chemical Physics, v. 133, p. 144501, doi: 10.1063/1.3495951.

Hammersley, A.P., Svensson, S.O., Hanfland, M., Fitch, A.N., Hausermann, D. (1996) Twp-Dimensional Detector Software: from real detector to idealized image or two-theta scan: High Pressure Research, v. 14, p. 235-248.

Hermann, J., Spandler, C., Hack, A., and Korsakov, A. (2006) Aqueous fluids and hydrous melts in high-pressure and ultra-high pressure rocks: Implications for element transfer in subduction zones: Lithos, v. 92, p. 399–417, doi: 10.1016/j.lithos.2006.03.055.

Horiuchi, H. and Sawamoto, H. (1981) β-Mg2SiO4: single crystal X-ray diffraction study: American Mineralogist, v. 66, p. 568-575

Hugh-Jones, D.A., and Angel, R.J. (1994) A compressional study of MgSiO3, orthoenstatite up to 8.5 GPa: American Mineralogist, v. 79, p. 405–410.

Irving, A.J. (1975) Subsolidus and melting relationships for calcite, magnesite and the join $CaCO_3$-$MgCO_3$ to 36 kb: Geochimica et Cosmochimica Acta, v. 39, p. 35–53.

Isshiki, M., Irifune, T., Hirose, K., Ono, S., Ohishi, Y., Watanuki, T., Nishibori, E., Takata, M., and Sakata, M. (2004) Stability of magnesite and its high-pressure form in the lowermost mantle: Nature, v. 427, p. 60–63, doi: 10.1038/nature02181.

Kaminsky, F., Wirth, R., Matsyuk, S., Schreiber, A., and Thomas, R. (2009) Nyerereite and nahcolite inclusions in diamond: evidence for lower-mantle carbonatitic magmas: Mineralogical Magazine, v. 73(5), p. 797-816.

Koziol, A.M., and Newton, R.C. (1998) Experimental determination of the reaction: Magnesite+ enstatite= forsterite+ CO_2 in the ranges 6-25 kbar and 700-1100 C: American Mineralogist, v. 83, p. 213–219.

Lay, T., Williams, Q., and Garnero, E.J. (1998) The core–mantle boundary layer and deep Earth dynamics: Nature, v. 392.6675, p.461-468.

Levien, L., and Prewitt, C.T. (1981) High-pressure crystal structure and compressibility of coesite: American Mineralogist, v. 66.3-4, p. 324-333.

Liu, J., Lin, J.-F., and Prakapenka, V.B. (2015) High-Pressure Orthorhombic Ferromagnesite as a Potential Deep-Mantle Carbon Carrier: Scientific Reports, v. 5, p. 7640, doi: 10.1038/srep07640.

Mao, H. K., J. Xu, and P. M. Bell. (1986) Calibration of the ruby pressure gauge to 800 kbar under quasi-hydrostatic conditions: Journal of Geophysical Research, v. 91.B5, p. 4673-4676.

Murakami, M. (2002) Water in Earth's Lower Mantle: Science, v. 295, p. 1885–1887, doi: 10.1126/science.1065998.

Nestola, F., and Smyth, J.R. (2016) Diamonds and water in the deep Earth: a new scenario: International Geology Review, v. 58, p. 263–276.

Ni, H., and Keppler, H. (2013) Carbon in Silicate Melts: Reviews in Mineralogy and Geochemistry, v. 75, p. 251–287, doi: 10.2138/rmg.2013.75.9.

Periotto, B., Balic-Zunic, T., Nestola, F., Katerinopoulou, A., and Angel, R.J. (2012) Re-investigation of the crystal structure of enstatite under high-pressure conditions: American Mineralogist, v. 97, p. 1741–1748, doi: 10.2138/am.2012.4157.

Poli, S., Franzolin, E., Fumagalli, P., and Crottini, A. (2009) The transport of carbon and hydrogen in subducted oceanic crust: An experimental study to 5 GPa: Earth and Planetary Science Letters, v. 278, p. 350–360, doi: 10.1016/j.epsl.2008.12.022.

Robie, R. A., B. S. Hemingway, and J. R. Fisher. (1978) Thermodynamic Properties of Minerals and Related Substances at 198.15 K and 1 Bar (10^5 Pascals) Pressure and at Higher Temperatures: Geological Survey Bulletin 1452: United States Government, Printing Office, Washington.

Ross, N.L., Shu, J.F., Hazen, R.M., and Gasparik, T. (1990) High pressure crystal chemistry of stishovite: American Mineralogist, v. 75, p. 739–747.

Ross, N.L. (1997) The equation of state and high-pressure behavior of magnesite: American Mineralogist, v. 82, p. 682–688.

Russell, J.K., Porritt, L.A., Lavallée, Y., and Dingwell, D.B. (2012) Kimberlite ascent by assimilation-fueled buoyancy: Nature, v. 481, p. 352–356, doi: 10.1038/nature10740.

Scott, H.P., Doczy, V.M., Frank, M.R., Hasan, M., Lin, J.-F., and Yang, J. (2013) Magnesite formation from MgO and CO2 at the pressures and temperatures of Earth's mantle: American Mineralogist, v. 98, p. 1211–1218, doi: 10.2138/am.2013.4260.

Shaw, A.M., Hilton, D.R., Fischer, T.P., Walker, J.A., and Alvarado, G.E. (2003) Contrasting He–C relationships in Nicaragua and Costa Rica: insights into C cycling through subduction zones: Earth and Planetary Science Letters, v. 214, p. 499–513, doi: 10.1016/S0012-821X(03)00401-1.

Shinmei, T., Tomioka, N., Fujino, K., Kuroda, K., and Irifune, T. (1999) In situ X-ray diffraction study of enstatite up to 12 GPa and 1473 K and equations of state: American Mineralogist, v. 84, p. 1588–1594.

Stagno, V., Tange, Y., Miyajima, N., McCammon, C.A., Irifune, T., and Frost, D.J. (2011) The stability of magnesite in the transition zone and the lower mantle as function of oxygen fugacity: Carbon/Carbonate fO_2 Buffer at High P: Geophysical Research Letters, v. 38, p. n/a–n/a, doi: 10.1029/2011GL049560.

Teweldeberhan, A.M., Boates, B., and Bonev, S.A. (2013) CO2 in the mantle: Melting and solid–solid phase boundaries: Earth and Planetary Science Letters, v. 373, p. 228–232, doi: 10.1016/j.epsl.2013.05.008.

Wyllie, P. J. (1980) The origin of kimberlite: Journal of Geophysical Research, v. B85.B12, p. 6902-6910.

Yoo, C.S., Cynn, H., Gygi, F., Galli, G., Iota, V., Nicol, M., Carlson, S., Häusermann, D., and Mailhiot, C. (1999) Crystal structure of carbon dioxide at high pressure: “Superhard” polymeric carbon dioxide: Physical Review Letters, v. 83, p. 5527.

APPENDIX A

PRE- AND POST-HEAT XRD PEAKS AND ASSOCIATED D-SPACINGS

.43 GPa Pre-heat NIU_008_DSP							.43 GPa Post-heat NIU_017_DSP						
observed d-spacing	reference d-spacing	Δd	observed phase	h	k	l	observed d-spacing	reference d-spacing	Δd	observed phase	h	k	l
1.749	1.749	0.000	forsterite	2	2	2	1.749	1.749	0.000	forsterite	2	2	2
1.947	1.949	0.003	forsterite	2	2	0	1.880	1.877	0.003	forsterite	1	5	0
2.053	2.032	0.021	forsterite	1	3	2	1.951	1.949	0.001	forsterite	1	3	2
2.160	2.160	0.000	forsterite	2	1	1	2.057	2.032	0.025	forsterite	1	2	2
2.272	2.269	0.003	forsterite	1	2	2	2.176	2.160	0.016	forsterite	2	1	1
2.454	2.459	0.005	forsterite	1	1	2	2.259	2.249	0.009	forsterite	1	4	0
2.518	2.512	0.006	forsterite	1	3	1	2.359	2.036	0.324	forsterite	0	4	1
2.769	2.768	0.001	forsterite	1	3	0	2.472	2.459	0.013	forsterite	1	1	2
3.004	2.993	0.011	forsterite	0	0	2	2.525	2.512	0.013	forsterite	1	3	1
3.495	3.498	0.003	forsterite	1	1	1	2.774	2.768	0.006	forsterite	1	3	0
3.730	3.724	0.006	forsterite	1	0	1	3.005	2.993	0.011	forsterite	0	0	2
3.885	3.885	0.000	forsterite	0	2	1	3.484	3.498	0.014	forsterite	1	1	1
							3.721	3.724	0.003	forsterite	1	0	1
							3.887	3.885	0.002	forsterite	0	2	1
2.43 GPa Pre-heat NIU_018_DSP							2.43 GPa Post-heat NIU_049_DSP						
observed d-spacing	reference d-spacing	Δd	observed phase	h	k	l	observed d-spacing	reference d-spacing	Δd	observed phase	h	k	l
1.737	1.741	0.004	forsterite	2	2	2	1.697	1.688	0.009	magnesite	1	1	6
1.897	1.882	0.015	CO_2	2	2	0	1.784	1.785	0.002	quartz	1	1	2
2.019	2.023	0.004	forsterite	1	3	2	1.930	1.924	0.005	magnesite	2	0	2
2.197	2.173	0.024	CO_2	2	1	1	2.089	2.087	0.002	magnesite	1	1	3
2.234	2.239	0.005	forsterite	1	4	0	2.196	2.197	0.001	quartz	1	1	1
2.259	2.259	0.001	forsterite	1	2	2	2.262	2.240	0.022	quartz	1	0	1
2.332	2.338	0.006	forsterite	0	4	1	2.415	2.413	0.002	quartz	1	1	0
2.406	2.381	0.025	CO_2	2	1	0	2.488	2.485	0.004	magnesite	0	0	6
2.455	2.448	0.007	forsterite	1	1	2	2.737	2.722	0.016	magnesite	1	0	4
2.498	2.501	0.004	forsterite	1	3	1	2.854	2.853	0.001	enstatite	6	1	0
2.755	2.756	0.000	forsterite	1	3	0	2.914	2.919	0.005	enstatite	3	2	1
2.976	2.980	0.004	forsterite	0	0	2	3.127	3.129	0.002	enstatite	2	2	1
3.111	3.074	0.037	CO_2	1	1	1	3.286	3.283	0.003	quartz	0	1	1
3.479	3.483	0.004	forsterite	1	1	1	3.479	3.483	0.004	forsterite	1	1	1
3.705	3.707	0.002	forsterite	1	0	1	3.698	3.707	0.009	forsterite	1	0	1
3.859	3.867	0.009	forsterite	0	2	1	3.858	3.867	0.010	forsterite	0	2	1

6.1 GPa Pre-heat NIU_060_DSP							6.1GPa Post-heat NIU_075_DSP						
observed d-spacing	reference d-spacing	Δd	observed phase	h	k	l	observed d-spacing	reference d-spacing	Δd	observed phase	h	k	l
1.725	1.728	0.002	forsterite	2	2	2	1.680	1.670	0.009	magnesite	1	1	6
2.128	2.072	0.056	forsterite	2	1	1	1.753	1.755	0.002	coesite	2	0	4
2.252	2.241	0.011	CO_2-III	1	1	2	1.941	1.949	0.008	enstatite	6	3	1
2.324	2.319	0.005	forsterite	0	4	1	2.082	2.066	0.016	magnesite	1	1	3
2.432	2.428	0.004	forsterite	1	1	2	2.145	2.127	0.018	forsterite	2	1	1
2.489	2.481	0.008	forsterite	1	1	1	2.254	2.241	0.013	forsterite	1	2	2
2.737	2.734	0.003	forsterite	1	3	0	2.307	2.320	0.013	forsterite	2	1	0
2.979	2.971	0.008	forsterite	1	2	1	2.453	2.459	0.006	magnesite	0	0	6
3.455	3.459	0.005	forsterite	1	1	1	2.625	2.649	0.024	coesite	1	3	1
3.678	3.681	0.004	forsterite	1	0	1	2.714	2.693	0.021	magnesite	1	0	4
3.837	3.831	0.006	forsterite	0	2	1	2.839	2.828	0.011	enstatite	6	1	0
							2.893	2.893	0.000	enstatite	3	2	1
							3.053	3.041	0.013	coesite	-2	2	1
							3.116	3.120	0.004	enstatite	2	2	1
							3.377	3.377	0.000	coesite	1	1	1
9.0 GPa Pre-heat NIU_083_DSP							9.0 GPa Post-heat NIU_091_DSP						
observed d-spacing	reference d-spacing	Δd	observed phase	h	k	l	observed d-spacing	reference d-spacing	Δd	observed phase	h	k	l
1.543	1.544	0.0004	forsterite	0	4	3	1.666	1.657	0.008	magnesite	1	1	6
1.722	1.717	0.004	forsterite	2	2	2	1.737	1.725	0.012	magnesite	0	2	4
2.068	2.062	0.005	ruby	1	1	3	1.811	1.791	0.020	clino-en	7	0	2
2.230	2.228	0.001	forsterite	1	2	2	1.912	1.915	0.002	clino-en	6	3	1
2.263	2.274	0.011	forsterite	2	1	0	1.949	1.942	0.006	clino-en	4	4	0
2.419	2.414	0.005	forsterite	1	1	2	2.071	2.066	0.005	magnesite	5	0	2
2.458	2.467	0.008	forsterite	1	0	1	2.249	2.259	0.009	magnesite	1	1	0
2.559	2.535	0.023	forsterite	0	2	2	2.287	2.274	0.013	forsterite	2	1	0
2.715	2.718	0.003	forsterite	1	3	0	2.447	2.440	0.007	magnesite	0	0	6
2.933	2.939	0.006	forsterite	0	0	2	2.693	2.693	0.000	coesite	2	2	0
3.418	3.417	0.001	forsterite	1	2	0	2.962	2.954	0.008	forsterite	1	2	1
3.658	3.656	0.002	forsterite	1	0	1	3.033	3.032	0.001	coesite	-4	0	2
3.809	3.814	0.005	forsterite	0	2	1	3.339	3.342	0.003	coesite	1	1	1

11.7 GPa Pre-heat NIU_094_DSP							11.7 GPa Post-heat NIU_104_DSP						
observed d-spacing	reference d-spacing	Δd	observed phase	h	k	l	observed d-spacing	reference d-spacing	Δd	observed phase	h	k	l
1.579	1.581	0.002	forsterite	1	3	3	1.513	1.514	0.001	stishovite	2	1	1
1.628	1.632	0.004	forsterite	2	4	1	1.576	1.581	0.005	forsterite	1	3	3
1.709	1.709	0.000	forsterite	2	2	2	1.650	1.647	0.003	magnesite	1	1	6
2.028	1.991	0.036	CO_2-III	2	1	1	1.739	1.716	0.023	magnesite	0	2	4
2.119	2.110	0.009	forsterite	2	1	1	1.849	1.849	0.001	stishovite	2	1	0
2.195	2.197	0.002	forsterite	1	4	0	1.899	1.879	0.020	magnesite	2	0	2
2.227	2.217	0.011	forsterite	1	2	2	1.901	1.910	0.009	clino-en	2	0	2
2.281	2.294	0.013	forsterite	0	4	1	1.945	1.954	0.008	clino-en	-3	3	1
2.411	2.402	0.009	forsterite	1	1	2	1.960	1.959	0.002	stishovite	1	1	1
2.449	2.454	0.006	forsterite	1	3	1	2.053	2.039	0.014	magnesite	1	1	3
2.697	2.704	0.007	forsterite	1	3	0	2.248	2.245	0.004	magnesite	1	1	0
2.880	2.816	0.065	CO_2-III	1	1	1	2.274	2.258	0.017	clino-en	2	0	2
2.929	2.924	0.005	forsterite	0	0	2	2.421	2.427	0.006	magnesite	0	0	6
3.415	3.417	0.002	forsterite	1	1	1	2.670	2.693	0.023	magnesite	1	0	4
3.647	6.637	2.990	forsterite	1	0	1	2.928	2.923	0.005	stishovite	1	1	0
3.776	3.795	0.018	forsterite	0	2	1	3.010	3.028	0.019	clino-en	2	2	0
15.4 GPa Pre-heat NIU_108_DSP							15.8 GPa Post-heat NIU_120_DSP						
observed d-spacing	reference d-spacing	Δd	observed phase	h	k	l	observed d-spacing	reference d-spacing	Δd	observed phase	h	k	l
1.712	1.693	0.019	forsterite	2	2	2	1.459	1.446	0.013	magnesite	2	1	1
1.814	1.821	0.007	forsterite	1	5	0	1.508	1.509	0.001	stishovite	2	1	1
2.006	1.992	0.014	CO_2-III	2	0	0	1.646	1.645	0.001	magnesite	1	1	6
2.197	2.183	0.015	forsterite	1	4	0	1.717	1.712	0.006	magnesite	0	2	4
2.389	2.386	0.003	forsterite	1	1	2	1.837	1.842	0.006	stishovite	2	1	0
2.427	2.438	0.011	forsterite	1	3	1	1.889	1.885	0.004	CO_2-III	2	0	2
2.682	2.686	0.004	forsterite	1	3	0	1.939	1.946	0.007	CO_2-III	1	1	2
2.842	2.905	0.063	forsterite	0	0	2	1.954	1.960	0.006	wadsleyite	2	4	0
3.402	3.395	0.007	forsterite	1	1	1	2.036	2.041	0.005	CO_2-IV	2	2	0
3.620	3.613	0.007	forsterite	1	0	1	2.052	2.034	0.019	magnesite	1	1	3
3.754	3.770	0.015	forsterite	0	2	1	2.175	2.180	0.005	CO_2-IV	0	3	3
							2.237	2.239	0.002	stishovite	1	0	1
							2.394	2.399	0.005	magnesite	0	0	6
							2.435	2.437	0.002	wadsleyite	1	3	2
							2.543	2.547	0.005	wadsleyite	2	1	1
							2.650	2.628	0.023	magnesite	1	0	4
							2.758	2.767	0.009	wadsleyite	2	0	1
							2.917	2.913	0.004	stishovite	1	1	0
							3.092	3.116	0.025	wadsleyite	1	1	2

21.1 GPa Pre-heat NIU_121_DSP							21.1 GPa Post-heat NIU_131_DSP						
observed d-spacing	reference d-spacing	Δd	observed phase	h	k	l	observed d-spacing	reference d-spacing	Δd	observed phase	h	k	l
1.569	1.574	0.005	forsterite	1	1	3	1.509	1.501	0.008	stishovite	2	1	1
1.693	1.682	0.011	forsterite	2	2	2	1.565	1.556	0.009	forsterite	1	3	3
1.750	1.741	0.009	forsterite	1	1	3	1.614	1.597	0.018	magnesite	0	1	3
1.797	1.804	0.007	forsterite	1	5	0	1.640	1.609	0.030	magnesite	1	1	6
1.964	1.954	0.010	forsterite	1	3	2	1.695	1.682	0.013	forsterite	2	2	2
2.114	2.110	0.004	CO_2-III	1	1	2	1.797	1.794	0.002	ringwoodite	3	2	1
2.156	2.163	0.006	forsterite	1	4	0	1.840	1.833	0.007	stishovite	2	1	0
2.191	2.182	0.009	forsterite	1	2	2	1.880	1.885	0.004	CO_2-III	2	0	2
2.255	2.258	0.002	CO_2-III	0	2	0	1.951	1.955	0.005	ringwoodite	4	0	0
2.379	2.364	0.015	forsterite	1	1	2	2.036	2.041	0.005	CO_2-IV	2	2	0
2.420	2.415	0.005	forsterite	1	3	1	2.146	2.163	0.016	forsterite	1	4	0
2.665	2.661	0.004	forsterite	1	3	0	2.191	2.182	0.010	forsterite	1	2	2
2.738	2.720	0.018	CO_2-III	1	1	1	2.232	2.205	0.027	stishovite	1	0	1
2.877	2.878	0.001	forsterite	0	0	2	2.372	2.375	0.003	forsterite	1	1	2
3.374	3.363	0.010	forsterite	1	1	1	2.422	2.415	0.007	forsterite	1	3	1
3.599	3.580	0.019	forsterite	1	0	1	2.472	2.483	0.010	forsterite	0	2	2
3.726	3.735	0.008	forsterite	0	2	1	2.628	2.593	0.035	magnesite	1	0	4
							2.663	2.661	0.002	forsterite	1	3	0
							2.713	2.720	0.007	CO_2-III	1	1	1
							2.904	2.895	0.009	CO_2-IV	2	0	2
							3.381	3.363	0.017	forsterite	1	1	1

APPENDIX B

MAGNESITE UNIT CELL PARAMETERS

a/a_0	c/c_0	V/V_0	P (GPa)
1	1	1	2.43
0.998438	0.985282	0.982207	6.1
0.978189	0.983042	0.940623	9
0.980407	0.972758	0.935009	11.7
0.97894	0.961611	0.92153	15.75
0.967968	0.92708	0.868641	21.1

APPENDIX C

MAGNESITE UNIT CELL PARAMETER TRENDLINE DATA

Unit Cell	a/a_o	c/c_o	V/V_o
slope	y = -0.0017x + 1.003	y = -0.0037x + 1.012	y = -0.0068x + 1.016
R^2	0.8232	0.9472	0.9597

APPENDIX D

THERMODYNAMIC MODELING OF REACTIONS 1 AND 2

Reaction 1 $2Mg_2SiO_4 + 3CO_2 = 3MgCO_3 + MgSiO_3 + SiO_2$	**CO_2 fluid T = 1500 K**										
	ΔSrxn1 (kJ/molK)	ΔHrxn1 (kJ/mol)	P (GPa)	ΔVrxn1 (cm^3/mol)	ΔVrxn1 (kJ/bar)	ΔGrxn1 (kJ/mol)	lnK	K	f_{CO2} (bars)	Entropy (S_{calc})	dP/dT	dT
	-0.6186	126.00										
			0.43	-74296	-74.30	1.05E+03	-8.42E+01	2.60E-37	1.57E+12	-27.46	-2706	-0.0002
			2.43	-74296	-74.30	-1.80E+06	1.44E+05	-	-	1377	53.94	0.0371
			6.1	-74291	-74.30	-4.53E+06	3.62E+05	-	-	3543	20.97	0.1750
			9	-74273	-74.30	-6.69E+06	5.34E+05	-	-	5383	13.80	0.2102
			11.7	-74269	-74.30	-8.69E+06	6.95E+05	-	-	7064	10.51	0.2568
			15.4	-74296	-74.30	-1.14E+07	9.15E+05	-	-	9289	7.998	0.4626
			21.1	-74305	-74.30	-1.57E+07	1.25E+06	-	-	12689	5.856	0.9734
	CO_2 solid T = 298 K											
	ΔSrxn1 (kJ/molK)	ΔHrxn1 (kJ/mol)	P (GPa)	ΔVrxn1 (cm^3/mol)	ΔVrxn1 (kJ/bar)	ΔGrxn1 (kJ/mol)	lnK	K	a_{CO2}	Entropy (S_{calc})	dP/dT	dT
	-0.527	-277.02										
			0.43	50.63	0.05	-1.20E+02	9.59E+00	1.46E+04	4.09E-02	0.4755	-106.5	-0.0040
			2.43	-23.54	-0.02	-6.92E+02	5.53E+01	1.05E+24	9.84E-09	2.164	10.88	0.1839
			6.1	-11.76	-0.01	-8.37E+02	6.69E+01	1.17E+29	2.05E-10	2.665	4.413	0.8316
			9	10.55	0.01	8.30E+02	-6.63E+01	1.56E-29	4.00E+09	-2.682	3.935	0.7370
			11.7	18.32	0.02	2.02E+03	-1.62E+02	5.86E-71	2.57E+23	-6.623	2.766	0.9763
			15.4	-38.70	-0.04	-6.08E+03	4.86E+02	1.10E+211	4.49E-71	19.92	1.943	1.905
			21.1	-14.59	-0.01	-3.20E+03	2.56E+02	1.07E+111	9.77E-38	10.45	1.396	4.084
Reaction 2 $Mg_2SiO_4 + 2CO_2 = 2MgCO_3 + SiO_2$	**CO_2 fluid T = 1500 K**										
	ΔSrxn1 (kJ/molK)	ΔHrxn1 (kJ/mol)	P (GPa)	ΔVrxn1 (cm^3/mol)	ΔVrxn1 (kJ/bar)	ΔGrxn1 (kJ/mol)	lnK	K	f_{CO2} (bars)	Entropy (S_{calc})	dP/dT	dT
	-0.4674	-141.66										
			0.43	-49530	-49.53	-2.12E+05	16979.94	-	-	641.1	77.26	-0.1459
			2.43	-49530	-49.53	-1.20E+06	9.62E+04	-	-	1535	32.26	-0.4020
			6.1	-49526	-49.53	-3.02E+06	2.41E+05	-	-	2362	20.97	0.1750
			9	-49537	-49.54	-4.46E+06	3.56E+05	-	-	3589	13.80	0.2101
			11.7	-49537	-49.54	-5.80E+06	4.63E+05	-	-	4710	10.52	0.2567
			15.4	-49535	-49.53	-7.63E+06	6.10E+05	-	-	6193	7.998	0.4626
			21.1	-49531	-49.53	-1.05E+07	8.35E+05	-	-	8694	5.697	1.001
	CO_2 solid T = 298 K											
	ΔSrxn1 (kJ/molK)	ΔHrxn1 (kJ/mol)	P (GPa)	ΔVrxn1 (cm^3/mol)	ΔVrxn1 (kJ/bar)	ΔGrxn1 (kJ/mol)	lnK	K	a_{CO2}	Entropy (S_{calc})	dP/dT	dT
	-0.365	-130.49										
			0.43	-14.82	-0.01	-85.505	6.83E+00	9.30E+02	3.28E-02	0.847	17.49	-0.6444
			2.43	-14.82	-0.01	-381.92	3.05E+01	1.81E+13	2.35E-07	1.927	7.692	-1.6861
			6.1	-6.42	-0.01	-413.40	3.30E+01	2.25E+14	6.67E-08	1.308	4.908	0.7478
			9	-14.74	-0.01	-1348.4	1.08E+02	6.48E+46	3.93E-24	4.381	3.364	0.8620
			11.7	-12.53	-0.01	-1488.2	1.19E+02	4.63E+51	1.47E-26	4.881	2.568	1.0513
			15.4	-22.18	-0.02	-3437.4	2.75E+02	2.15E+119	2.16E-60	11.260	1.970	1.8783
			21.1	1.56	0.00	306.39	-2.45E+01	2.31E-11	2.08E+05	-0.998	1.558	3.6591